

From cell to atomic level: Understanding the Degradation in 99% Coulombic Efficiency and 450 Wh kg⁻¹ Anode-Free Pouch Cells

Lei Liu^{2,4,5} Yuxuan Xiang^{1,4,*} and Jianhui Wang^{1,2,3,4*}

¹Research Center for Industries of the Future (RCIF), Westlake University, Hangzhou 310030, China.

²Key Laboratory of 3D Micro/Nano Fabrication and Characterization of Zhejiang Province, School of Engineering, Westlake University, Hangzhou 310030, China.

³Division of Solar Energy Conversion and Catalysis at Westlake University, Zhejiang Baima Lake Laboratory Co. Ltd., Hangzhou 310000, China

⁴Institute of Advanced Technology, Westlake Institute for Advanced Study, Hangzhou 310024, China.

⁵School of Materials Science and Engineering, Zhejiang University, Hangzhou, 310027, China.

*Corresponding Author: Yuxuan Xiang, Jianhui Wang

xiangyuxuan@westlake.edu.cn; wangjianhui@westlake.edu.cn

Summary

Anode-Free Lithium Metal Batteries (AFLMBs) promise ultra-high energy densities beyond 500 Wh kg⁻¹, yet a significant gap from prior studies mainly limited to <350 Wh kg⁻¹, which lacks advantages over commercial Li-ion batteries and mechanistic understanding of battery degradation at high-energy levels. Here we developed Ah-level 450 Wh kg⁻¹ AFLMBs with >99% coulombic efficiency and examined their degradation comprehensively. Under high-energy conditions, battery degradation behavior is dictated by the major inactive lithium component, and the solid electrolyte interphase (SEI) flexibility proves more vital than Young's modulus for lithium metal stabilization. Two typical modes of "sudden death" and "gradual decay" are revealed, which associate with "truffle-shaped" dead lithium caused by brittle SEI and "mushroom-shaped" active lithium interwoven with flexible SEI, respectively. The SEI-dominated gradual-decay mode, with slower degradation and minimized dead lithium, exhibits superior lifespan and safety. These insights, contrasting with previous lower-energy-density battery studies, provide crucial guidance for developing practical, high-energy-density, and safe AFLMBs.

Keywords: Anode-free lithium metal battery, 450 Wh kg⁻¹ pouch cell, failure mechanism, SEI, dead lithium

Introduction

Over recent decades, the pervasive adoption of lithium-ion batteries has profoundly influenced our daily life, catalyzing the emergence of numerous battery-dependent sectors, including mobile communications, portable computing, and the burgeoning field of electric vehicles with the escalating demand for higher energy-dense batteries. This triggers worldwide interest in replacing traditional graphite anodes with higher energy density alternatives like silicon anodes, lithium metal anodes, and, ultimately, anode-free lithium metal batteries (AFLMBs).¹⁻⁸ AFLMBs, characterized by their fully lithiated cathode and bare copper current collectors, promise notable advantages, including: (1) exceptional energy densities potentially surpassing 500 Wh kg^{-1} , attributable to a more compact battery configuration; (2) reduced manufacturing costs by eliminating the conventional anode materials; (3) enhanced safety due to the absence of excessive chemically reactive lithium metal; (4) the facile recycling of the economically valuable copper current collector; and (5) highly compatibility with established manufacturing process of lithium ion batteries. However, AFLMBs encounter great challenges in longevity, as parasitic reactions between plated Li metal and electrolytes irreversibly deplete the limited lithium supply, which impedes their practical applications.^{8,9}

Recent research has focused on prolonging AFLMB cycle life through novel electrolyte designs¹⁰⁻¹⁵ and current collector modifications.¹⁶⁻¹⁹ Current AFLMB research predominantly showcases energy densities between 50 and 350 Wh kg^{-1} , with typical lifespans of 50–150 cycles at 80% capacity retention.⁸⁻¹⁹ Implementing lithium compensation strategies on the cathode side, such as discharge depth²⁰ control and Li_2O additives,²¹ can extend lifespan to 200–300 cycles. However, such AFLMBs do not exhibit remarkable advantages in energy density or lifespan compared to commercial lithium-ion batteries using graphite or Si/C anode ($160\text{--}350 \text{ Wh kg}^{-1}$). Therefore, priority should be given to the development of AFLMBs exceeding 400 Wh kg^{-1} , a level challenging for conventional lithium-ion batteries. Yet, research on AFLMBs at this energy level is scarce, and their lifespans remain quite short (<100 cycles).^{22,23} This underscores the pressing need to improve the cycle life of 400 Wh kg^{-1} -level AFLMBs.

Understanding the battery degradation is crucial for developing high-energy-density, practical AFLMBs. So far, various factors have been identified as influencing AFLMB performances, such as electrolyte depletion,²⁰ Li metal corrosion,²⁴ continuous loss of active Li,²⁵ solvation structure

change,²⁶ accumulation of dead crystalline Li,²⁷ generation of LiH,²⁸ large LiOH crystal²⁹ and gas product,³⁰ and transition metal dissolution³¹ (Supplementary Table 1), yet the primary determinant remains elusive. This divergence in views likely stems from the considerable variance in energy densities (50–350 Wh kg⁻¹) of the batteries studied and the limited research scope that usually focuses on individual facets rather than a systematic comparison. Low-energy-density coin cells, characterized by a surplus of electrolyte, low cathode mass-loading, and relatively thin plated/stripped lithium metal layers, exhibit degradation behaviors markedly different from those of high-energy-density pouch cells (see **Fig. 1a**).^{3,32} In addition, many mechanistic studies employed conventional electrolytes with a lithium plating/stripping Coulombic efficiency (CE) of less than 99%, which may enable cycles in low-energy-density AFLMBs but fail to support a reversible charge/discharge in >400 Wh kg⁻¹ AFLMBs due to severe dendritic short-circuiting. Hence, failure mechanisms identified in low-energy-density batteries cannot be directly applied to their high-energy-density counterparts.

Moreover, it should be noted that battery configurations for > 400 Wh kg⁻¹ AFLMBs necessitate ultra-high cathode mass-loading (>5.0 mAh cm⁻²), lean electrolytes (<3.0 g Ah⁻¹), and rigorous specifications for ultra-thin separators and current collectors. In such stringent conditions, the factors influencing the battery degradation process, such as electrolyte consumption, dendrite growth, accumulation of inactive Li, SEI properties, and cross talk between cathode and anode, are likely to exhibit interactive relationships, further complicating the degradation dynamics. Therefore, to untangle these factors, it is necessary to conduct a systematic and comprehensive mechanistic investigation on practical AFLMBs under stringent conditions.

In this study, we employed a high-energy-density nickel-rich NCM811 cathode (216 mAh g⁻¹ at 4.4 V) alongside advanced electrolytes of >99% CE, including all-fluorinated electrolyte (AFE) and localized high-concentration electrolyte (LHCE), to construct anode-free pouch cells. These cells attained an energy density of 450 Wh kg⁻¹ at the ampere-hour (Ah) level, featuring ultra-high cathode mass-loading (5.6 mAh cm⁻²) and minimal electrolyte usage (2.0 g Ah⁻¹) (**Fig. 1a**). We carried out a systematic investigation into the performance degradation of these high-energy-density AFLMBs across various dimensions, including the cell, electrode, and atomic levels. This included analyzing variations in cell capacity, coulombic efficiency, impedance, and thickness; morphological changes

in electrodes and separator; and compositional and mechanical evolution of interphases (~ 10 mg), along with a quantitative assessment of inactive Li (see **Fig. 1b**). Through this comprehensive methodological analysis, we successfully elucidated the correlation among the battery decay behavior, lithium metal morphology evolution, dominant inactive component, and interphase properties for practical 450 Wh kg^{-1} AFLMBs for the first time, offering insights that will advance the development of high-performance AFLMBs.

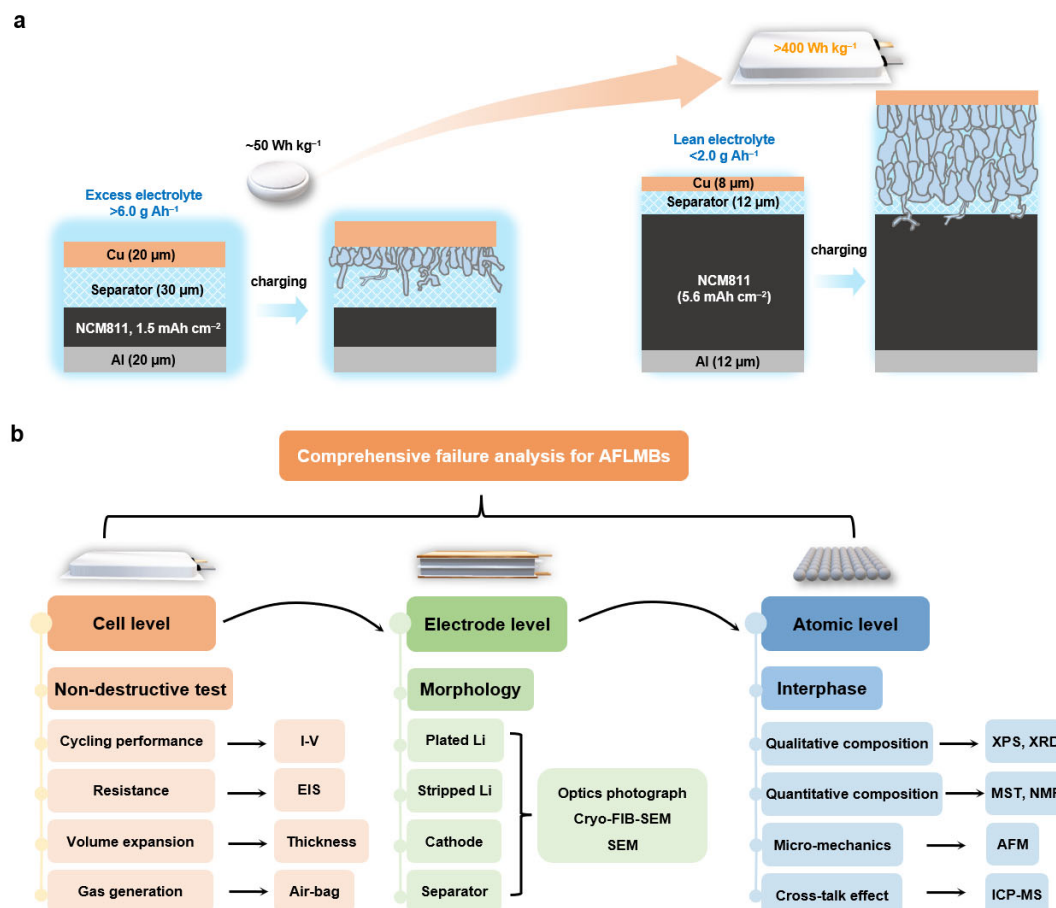


Figure 1. Cell configurations and failure analysis for AFLMBs. (a) Schematic illustration of AFLMB configurations under low and high energy density conditions. (b) Flowchart of failure mechanism analysis for practical anode-free lithium metal pouch cells. Note that for high-energy-density pouch cells, due to the thick lithium deposition layer and coarse lithium grains, Cryo-EM is not suitable for this study.

Results

Cell level

The tested AFLMBs consist of dual layers of double-coated NCM811 cathode and triple layers of Cu foils, with a capacity of 0.54 Ah and an energy density of 450 Wh kg^{-1} . Detailed specifications of the

battery parameters are provided in Supplementary Table 2. Prior studies have shown the significant impact of external pressure on battery performance; however, the application of excessively high pressure necessitates specialized pressurizing apparatus, leading to increased costs and a reduction in the systematic energy density.³³ Thus, for practicality, all AFLMBs were tested under a moderate pressure of 200 kPa. The charge/discharge current densities were set at 0.2C/0.5C, respectively. Given the high cathode loading (5.6 mAh cm^{-2}), 0.2C corresponds to a current density as high as 1.12 mA cm^{-2} . In such harsh conditions, the cycling performances significantly deviate from those of low-energy-density AFLMBs. Although both AFE and LHCE achieved over 300 cycles in Li||Cu coin cells with an average coulombic efficiency (CE) exceeding 99% (Supplementary Fig. 1), the lifespan of the 450 Wh kg^{-1} pouch cells were limited to merely 20 and 38 cycles (80% capacity retention) for AFE and LHCE, respectively. When comparing to 350 Wh kg^{-1} AFLMB using LHCE (100 cycles),²⁵ this lifespan is dramatically reduced into less half. For commercial electrolyte (CME: 1.0 M LiPF₆ in EC/DMC) with 92% average CE in Li||Cu coin cells, a short circuit occurred even in the first charge to 4.1 V in the 450 Wh kg^{-1} pouch cell, failing to support a reversible charge/discharge cycle (Supplementary Fig. 1). The discrepancy in cycle performance reflects a different failure process in AFLMBs under conditions of high versus low energy density.

As shown in **Fig. 2a,b**, for AFE batteries, the CE sharply dropped from 99.4% to below 90% after just 24 cycles, accompanied by a marked increase in polarization in the charge/discharge curves, indicative of a “sudden-death” failure. In contrast, the LHCE batteries achieved 99% average CE within the initial 45 cycles and preserved a CE above 95% after 80 cycles, accompanied by a gradual increase in polarization, reflecting a “gradual-decay” failure (**Fig. 2a,c**). Throughout the cycling process, neither battery experienced short circuit or gas generation, but significant volume expansion was observed (Supplementary Fig. 2). The percentages of volume expansion in 40 cycles increased to be 21.1% for AFE and 18.4% for LHCE batteries, respectively (**Fig. 2d**), suggesting the presence of materials unstable in both batteries.

Electrochemical impedance spectroscopy (EIS) was utilized to monitor the impedance changes in the cycling. The AFE battery exhibited a noticeable increase in internal resistance (R_0), SEI impedance (R_1), and interfacial reaction impedance (R_2) within the first 20 cycles (**Fig. 2e,f**). The pronounced rise in R_0 , influenced by the conductivity of the electrolyte, suggests significant

electrolyte consumption during 5–20 cycles in the AFE battery. Conversely, the LHCE battery showed less apparent changes during the initial 20 cycles, indicating relative stability during this period (**Fig. 2e,f**). These observations delineate two distinct yet typical degradation processes of AFLMBs under this high-energy-density condition. To probe the underlying causes, we disassembled the batteries for a more detailed investigation at the electrode level.

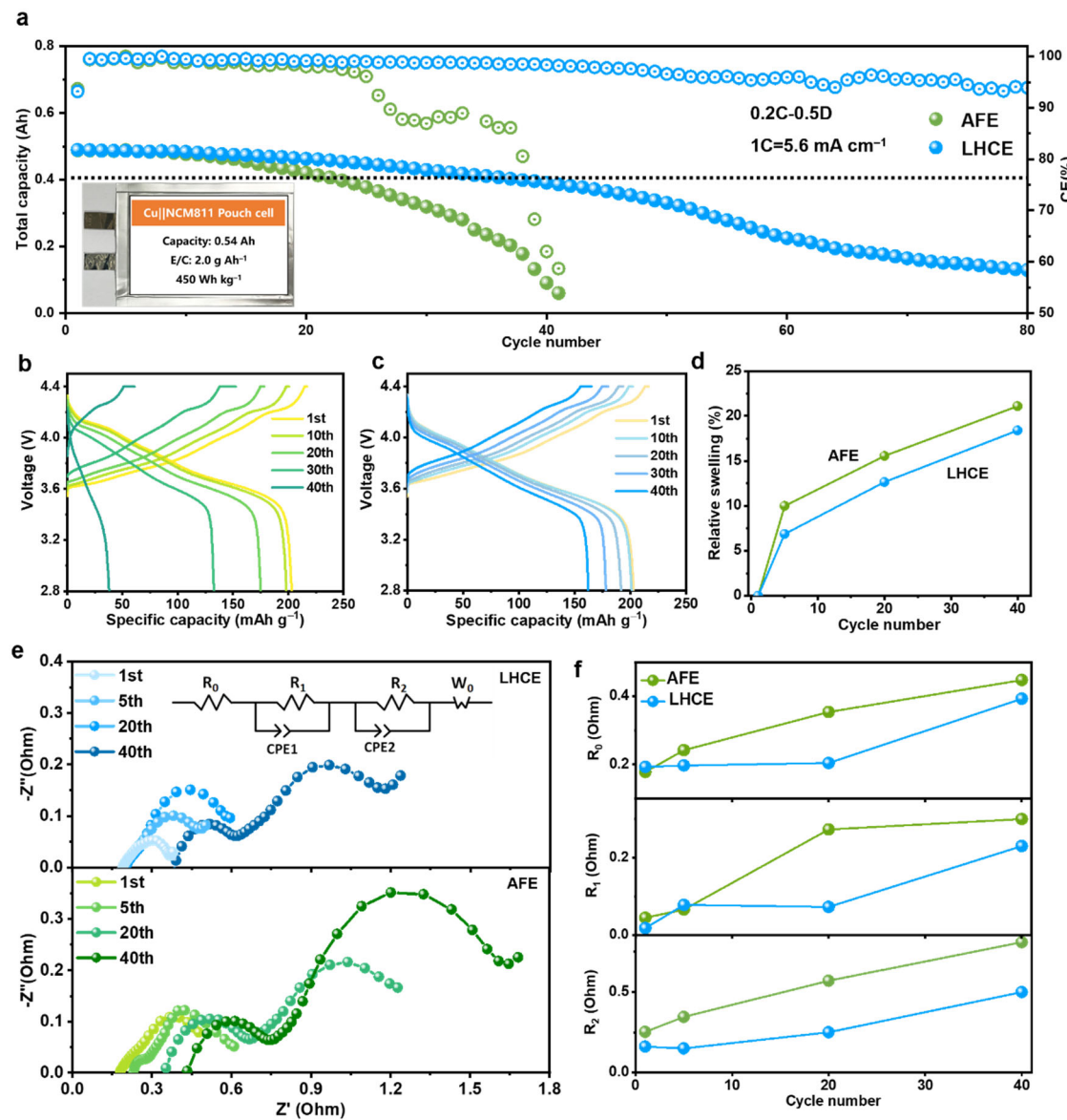


Figure 2. Electrochemical performances of 450 Wh kg⁻¹ AFLMBs. (a) Cycling stability of AFLMBs using electrolytes of AFE and LHCE. Insert: Optical image of a 450 Wh kg⁻¹ AFLMB. (b, c) Charge and discharge curves of the AFLMBs at different cycles in AFE (b) and LHCE (c). (d) The variance of AFLMB thickness during cycling. The cell expansion percentage is calculated by dividing the increased thickness during cycling by that in initial charged state (e) Nyquist plots of the AFLMBs during cycling and the corresponding evolution of ohmic (R_0), SEI (R_1) and charge transfer (R_2) resistances.

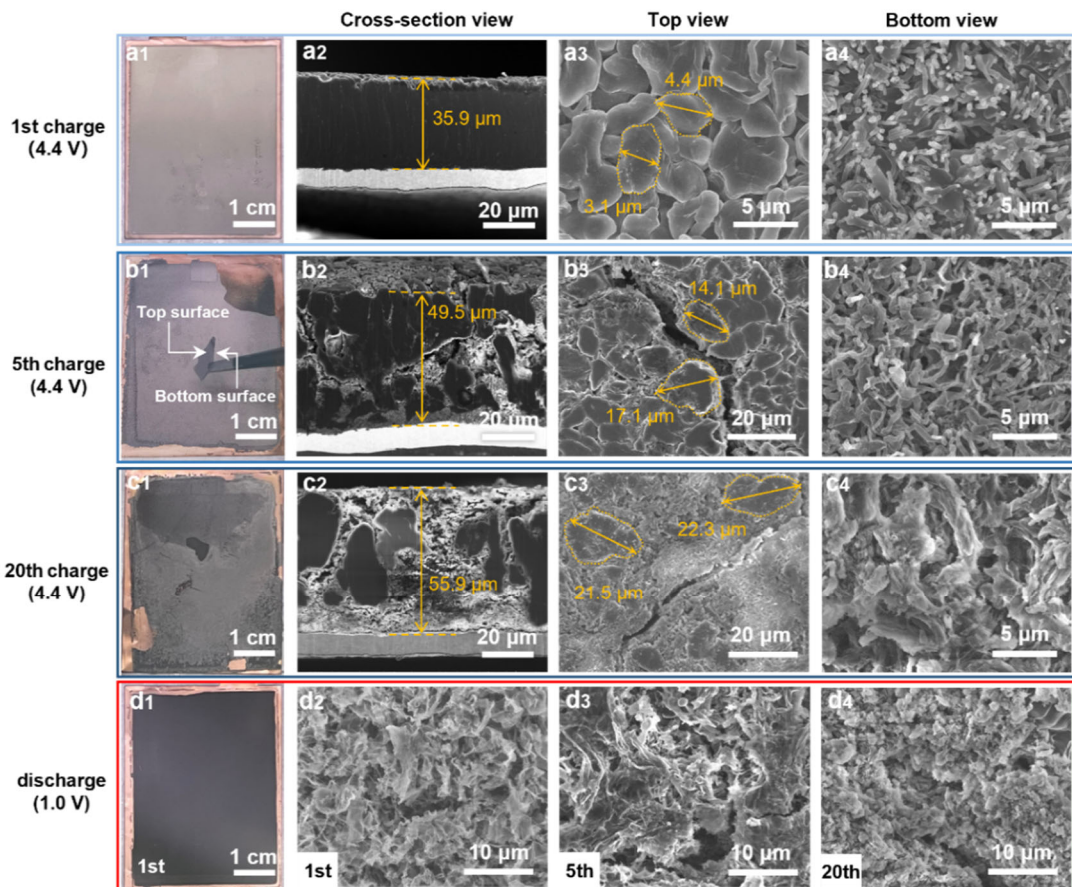


Figure 3. Morphology evolution of plated/stripped lithium layers in the 450 Wh kg⁻¹ AFLMB using AFE. (a-c) Morphologies of plated lithium (5.6 mAh cm⁻²) at 1st, 5th, and 20th cycle, respectively: (a1-c1) optical images, (a2-c2) cross-sectional cryo-FIB-SEM images, (a3-c3) top-view SEM images, and (a4-c4) bottom-view SEM images of the plated lithium layer. (d1) Optical image at 1st fully stripped state. (d2-d4) SEM images at 1st, 5th and 20th fully stripped states, respectively.

Electrode level

Upon disassembling the failed pouch cells, we observed that the morphology of NCM811 cathode materials in both batteries remained largely unchanged, as depicted in Supplementary Fig. 3–5. When these cycled cathode materials were paired with fresh lithium metal, they demonstrated a resumable specific capacity of 216 mAh g⁻¹ (Supplementary Fig. 5), signifying no degradation of the cathode materials during the cycling. Hence, our investigation shifted focus towards the anode side.

Figure 3 illustrates the morphological evolution of the lithium-plated and lithium-stripped anodes in the AFE batteries after 1st, 5th, and 20th cycles. From **Fig. 3a1–c1**, a progressive dimming of metallic sheen in the plated lithium was observed over 1–20 cycles. The plated lithium metal became noticeably fragile, easily fracturing upon minimal blending, indicating its brittle mechanical

property. An evident increase in the lithium layer thickness was observed from the cross-section views (**Fig. 3a2–c2**): 35.9 μm (1st) \rightarrow 49.5 μm (5th) \rightarrow 55.9 μm (20th), accompanied by a dramatically increase of pulverized components. Meanwhile, continuous surface cracking and pulverization, along with an enlargement in the particle size of the plated lithium, was clearly visible from the top views (adjacent to the electrolyte side) (**Fig. 3a3–c3**, Supplementary Fig. 6). After 20 cycles, portions of the plated lithium had even detached from the Cu current collector, adhering to the separator (Supplementary Fig. 3). Moreover, numerous microcracks were present on the anode surface, even in 1st fully stripped state (**Fig. 3d2**), further confirming the brittle nature of the AFE-derived SEI. Additionally, a marked difference was noted in the morphology between the top surface (adjacent to the electrolyte) and the bottom surface (nearest to the Cu foil) of the plated lithium layer. Initially, the upper surface was composed of 3–5 μm lithium grains (**Fig. 3a3**), consistent with previous reports.¹⁰ Unexpectedly, the bottom surface exhibited a distinct nano-sized needle-like morphology (**Fig. 3a4**). These needle-like lithium structures transformed into laterally expanding lithium dendrites within just 5 cycles (**Fig. 3b4**), ultimately evolving into coarse and pulverized components (**Fig. 3c4**). Such initial uneven lithium nucleation and growth, along with brittle SEI cracking, likely exposed fresh lithium metal to the electrolyte, leading to continuous electrolyte consumption during the cycling. Concurrently, the deterioration in contact between the plated lithium metal and the current collector could further exacerbate uneven lithium deposition and the accumulation of inactive lithium (**Fig. 3**, Supplementary Fig. 3, 6, 7).

Conversely, the plated lithium metal layer in the LHCE battery retained its metallic sheen throughout 20 cycles (**Fig. 4a1–d1**). It exhibited no fractures when subjected to a 180-degree bend (**Fig. 4a1–b1**) and remained intact over 20 cycles (**Fig. 4c1–c3**, Supplementary Fig. 8), indicating a highly flexible mechanical property. Upon complete stripping, the lithium metal contracted without forming cracks, instead developing a three-dimensional porous structure (**Fig. 4e1–e4**, Supplementary Fig. 9), a characteristic markedly distinct from that observed in the AFE battery. Moreover, significant differences were noted between the top and bottom surfaces of the plated lithium layer, similar to observations in the AFE battery. Initially, the top surface featured 4–8 μm lithium grains (**Fig. 4a3**), whereas the bottom surface was covered with laterally expanding dendritic structures (**Fig. 4a4**). Despite the appearance of pulverization on the lithium metal surface as cycling

advanced (**Fig. 4a3–d3**), the overall morphology, including the top, bottom and cross-section views, remained more stable compared to the AFE battery (Fig. 3, 4). Thus, under identical testing conditions, the plated lithium in LHCE battery was denser and thinner than that in the AFE battery (**Fig. 4a2–c2**).

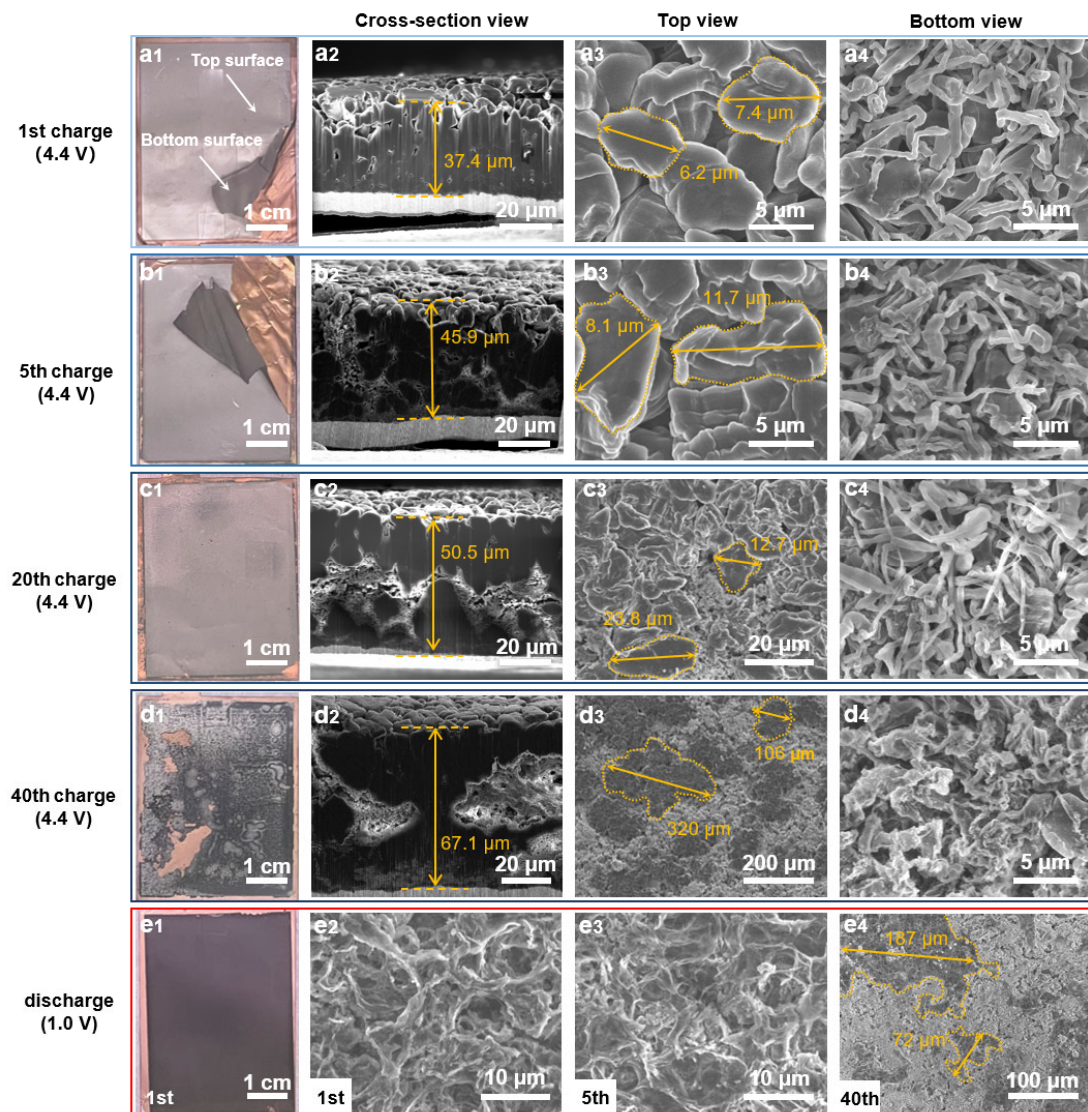


Figure 4. Morphology evolution of plated/stripped lithium layers in the 450 Wh kg⁻¹ AFLMB using LHCE. (a-d) Morphologies of plated lithium (5.6 mAh cm⁻²) at 1st, 5th, 20th and 40th cycle, respectively: (a1-d1) optical images, (a2-d2) cross-sectional cryo-FIB-SEM images, (a3-d3) top-view SEM images, and (a4-d4) bottom-view SEM images of the plated lithium layer. (e1) Optical image at 1st fully stripped state. (e2-e4) SEM images at 1st, 5th and 40th fully stripped states, respectively.

Upon comparing **Fig. 3** with **Fig. 4**, the initial lithium deposition morphologies of the two batteries were quite similar (**Fig. 3a1–a4** vs. **Fig. 4a1–a4**). However, with a 20% capacity degradation, they diverged into different morphologies (**Fig. 3c1–c4** vs. **Fig. 4d1–d4**). The top-view and cross-sectional images reveal that the plated lithium in the AFE battery assumed columnar crystal

formations approximately 10–20 µm in diameter (**Fig. 3c2,c3**). Conversely, the plated lithium in the LHCE battery evolved into large-sized island-shaped structures with diameters ranging from 100 to 400 µm, which encompassed large-sized pulverized components within the plated lithium layer (**Fig. 4d2,d3**). Cryogenic focused ion beam scanning electron microscopy (Cryo-FIB-SEM) dissection of these island-shaped lithium structures (**Fig. 5a–c**) show that the upper part of plated lithium layer remained largely intact during the FIB process, whereas the lower and middle parts gradually diminished and vanished, giving rise to a “mushroom-shaped” morphology. In the subsequent discharge, these “mushroom-shaped” lithium was stripped, leaving behind a pattern of porous cavities (indicated by dotted line in **Fig. 5d–f**) within the thick pulverized layer. In stark contrast, numerous dead lithium particles in 10–30 µm diameter were clearly observed in the 40th fully stripped lithium layer in the AFE battery (**Fig. 5g**). These seemingly dense metallic lithium particles were enveloped by a thick pulverized matrix (**Fig. 5h**), resembling “truffle” buried in soil, and consequently lost essential contact with the current collector (**Fig. 5i**), rendering them non-oxidizable during the discharge process.

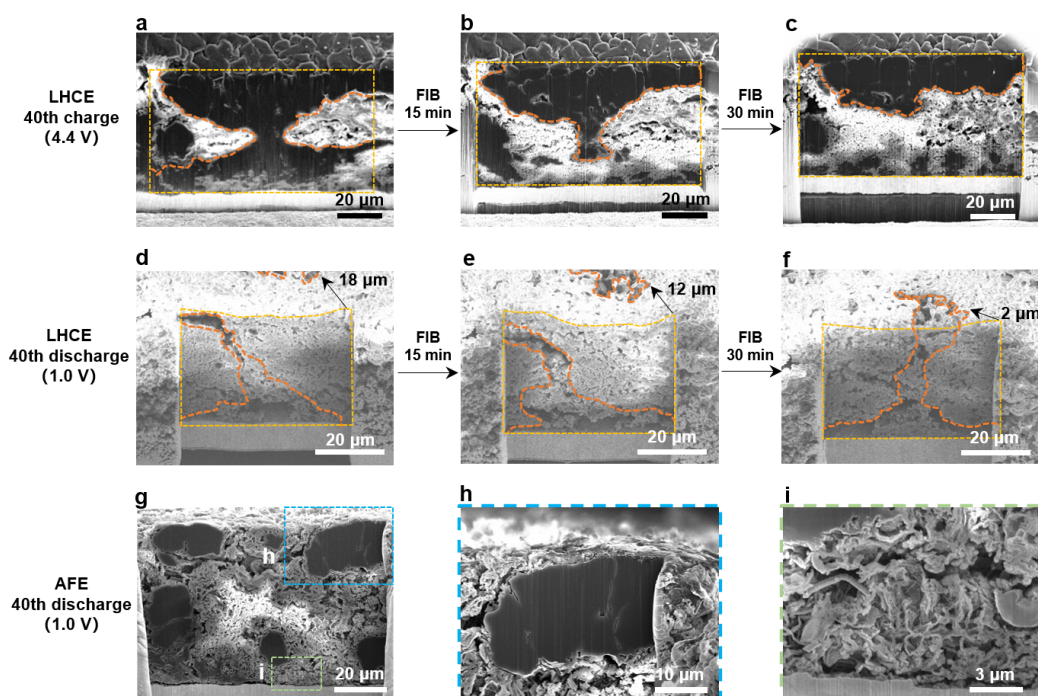


Figure 5. Morphology evolution of the 40th plated/stripped lithium layer upon Cryo-FIB continuous milling. (a–c) Cross-section image slices for the 40th plated lithium layer in the LHCE AFLMB with increasing the milling distance. The plated active lithium presents a “mushroom-shaped” morphology. (d–f) Cross-section image slices for the 40th stripped lithium layer in the LHCE AFLMB with increasing the milling distance. (g–i) Cross-section image for the 40th plated lithium layer in the AFE AFLMB. (h, i) are magnified views in (g). The dead lithium particles were buried in the “soil-like” SEI, showing a “truffle-shaped” morphology.

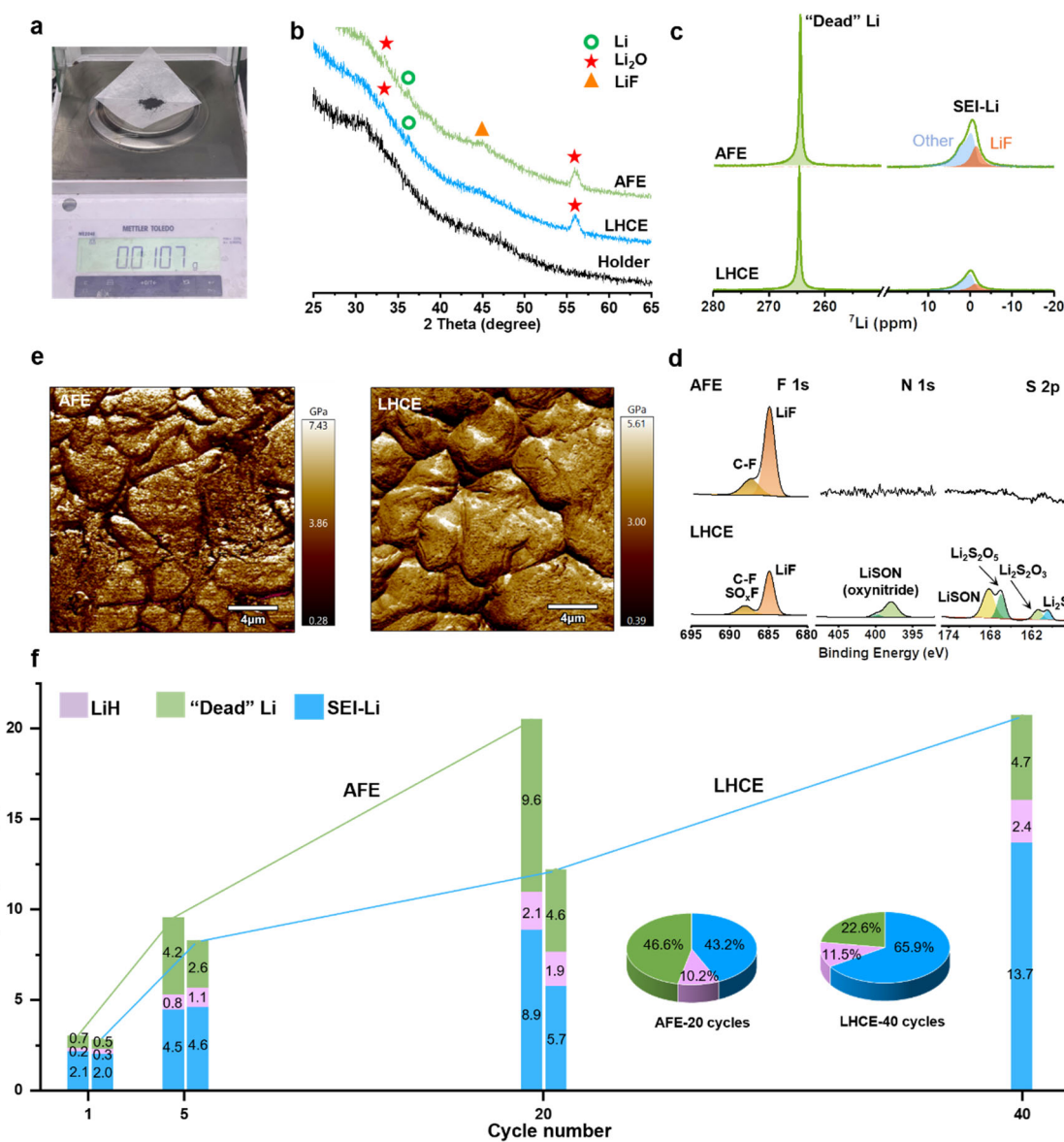


Figure 6. Structural characterizations and quantitative compositional analysis of inactive lithium. (a) “Ten milligram-level” inactive lithium sample collected from 5th fully stripped current collector. (b) XRD analysis of ~10.7 mg inactive lithium samples after 5 cycles. (c) ⁷Li NMR spectra of inactive lithium samples after 5 cycles. (d) XPS spectra of inactive lithium samples after 5 cycles. (e) AFM Young’s modulus distributions for 5th plated Li layers. (f) Quantitative analysis of inactive lithium by the mass spectrometry titration. The capacity loss consumed by three kinds of inactive lithium (LiH, “dead” Li and SEI-Li) is normalized by the first charge capacity. The inset pie chart represents the relative contents of these three inactive lithium at around 20% capacity loss.

Atomic level

To delve into the detailed evolution in lithium plating/stripping throughout the cycling, a range of analytical techniques was systematically utilized to explore the compositional and microstructural changes in inactive lithium after complete delithiation in AFLMBs (discharged to 1.0 V,

Supplementary Fig. 10). Note that for high-energy-density pouch cells, due to the thick lithium deposition layer and coarse lithium grains, the widely used Cryo-Electron Microscopy (Cryo-EM) proves less suitable for such analyses. The simplified configuration of AFLMBs enabled the extraction of over 10 mg of inactive lithium from the Cu current collector (**Fig. 6a**), thereby making conventional X-ray diffraction (XRD) analysis possible. As depicted in **Fig. 6b** and Supplementary Fig. 11, the inactive lithium harvested from AFLMBs after 5 cycles demonstrated a predominantly amorphous state, regardless of the electrolyte composition. A minor presence of crystalline lithium metal, Li₂O, and LiF was detected. Among them, the lithium metal identified post-full delithiation is classified as dead Li, while LiF and Li₂O are commonly recognized SEI components (denoted as SEI-Li).^{2,34} Clearly, the AFE battery showed higher concentrations of dead Li and LiF. Quantitatively analysis via Nuclear Magnetic Resonance (NMR) ⁷Li spectra (**Fig. 6c**) provided estimates for the molar ratio of dead Li (260 ppm) and LiF (-1.3 ppm) in the inactive lithium. For the AFE battery, the relative contents of dead Li and LiF were 44% and 19%, respectively, compared to 31% and 7% for the LHCE battery. This indicates that the content of LiF in the AFE sample was 2.7 times that of the LHCE sample, corroborating XRD results. X-ray Photoelectron Spectroscopy (XPS) and Atomic Force Microscopy (AFM) analyses were conducted to directly assess the composition and mechanical properties of the SEI on Cu. The F1s XPS spectrum confirmed a higher LiF concentration in the AFE-derived SEI,^{10,35} whereas the N1s and S2p XPS spectra demonstrated the presence of unique N- and S-species in the LHCE-derived SEI (**Fig. 6d**).^{11,36,37} AFM analysis across a substantial area of 20×20 μm (**Fig. 6e**) reveals a higher Young's modulus in the AFE-derived SEI (3.86 vs. 3.0 GPa), likely associated with its increased LiF content.^{2,38,39} Paradoxically, despite the augmented LiF concentration and the elevated Young's modulus of the AFE-derived SEI compared to the LHCE-derived SEI, the AFE battery produced more dead Li after 5 cycles.

In addition to dead Li and SEI-Li, lithium hydride (LiH) has been identified as another significant factor contributing to the consumption of active Li in batteries.⁴⁰⁻⁴³ To thoroughly investigate the battery's degradation process, heavy water (D₂O) was utilized to react with inactive lithium components. Both dead Li and LiH react with D₂O, producing D₂ and HD gases, which was quantitatively analyzed through mass spectrometry. The establishment of standard and titration curves for inactive Li is shown in Supplementary Fig. 12. The methodology for calculating the content of

dead Li, LiH and SEI-Li is detailed in the experimental section. **Fig. 6f** presents the evolution of various inactive lithium species that collected from the 450 Wh kg⁻¹ pouch cells across the initial 20% capacity decay process. In the first cycle, the capacity loss in both batteries was primarily caused by SEI-Li (~2%), along with negligible dead Li (0.7% for AFE, 0.5% for LHCE) and LiH (0.2% for AFE, 0.3% for LHCE). After 5 cycles, the capacity loss by dead Li formation quickly increased to 4.2% in AFE battery, which is comparable to capacity loss by SEI-Li (4.5%). After 20 cycles, the contribution of dead Li (9.6%) exceeded that of SEI-Li (8.9%) in AFE battery, accounting for 46.6% of the total inactive Li (**Fig. 6f inset**), thus emerging as the culprit of active Li consumption, in line with the observation in cryo-FIB-SEM results (**Fig. 5c**). In stark contrast, dead Li accumulation in the LHCE battery increased more steadily over the cycles. After 40 cycles, the capacity loss due to dead Li accounted for only 4.7%, while SEI-Li contributed to 13.7%, making up 65.9% of total inactive Li (**Fig. 6f inset**), aligning with observations from **Fig. 5a,b**. Contrary to previous reports,⁴⁰⁻⁴³ our findings indicate that the LiH component in the inactive Li of both batteries retained relatively low proportions (<2.4%) throughout the whole cycling, showing a minor effect on active Li loss until battery failure. In addition, Inductively Coupled Plasma Mass Spectrometer (ICP-MS) analysis was conducted to measure the levels of transition metals (Ni, Co, Mn) within the SEI. Detected concentrations of these metals in both batteries were below 0.12 ppm (**Fig S12**), far below >5.0 ppm commonly reported in the literatures.^{37,44,45} This ICP result rules out the possible influence of crosstalk effect caused by transition metal dissolution. Consequently, for 450 Wh kg⁻¹ AFLMBs, the apparent primary factors in capacity decay are identified as the accumulaiton of SEI-Li and/or dead Li during cycling.

Discussion

Through the detailed analysis conducted across cell, electrode, and atomic levels, we have unveiled the evolution of electrochemical behaviors, electrode structure/morphology, and interphase composition in practical high-energy-density AFLMBs throughout their cycling life. This comprehensive exploration enables us to engage in an in-depth discussion from three distinct perspectives as follows.

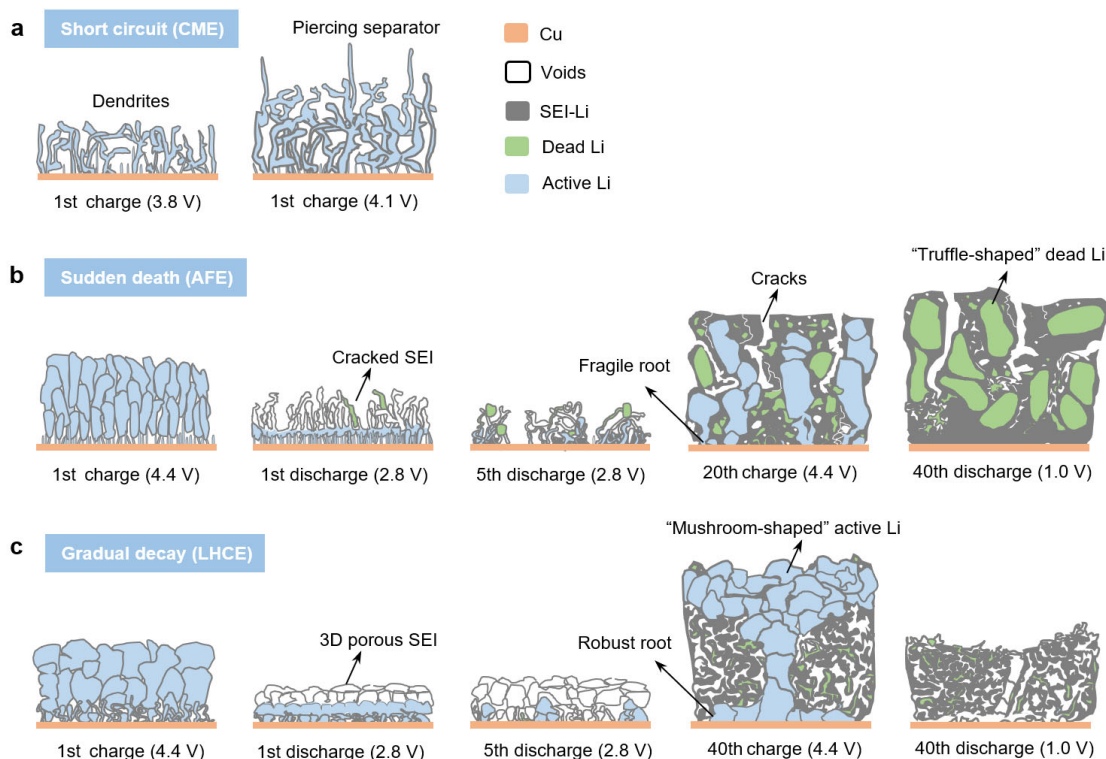


Figure 7. Schematic illustration of different failure models for 450 Wh kg⁻¹ AFLMBs. (a) Short circuit, **(b)** Sudden death and **(c)** Gradual decay.

Firstly, the major inactive lithium component dictates the failure behaviors under practical high-energy conditions. Employing advanced electrolytes with a CE exceeding 99%, this work successfully developed 450 Wh kg⁻¹ AFLMBs with minimal electrolyte dose (2.0 g Ah⁻¹) and ultra-high cathode loading (5.6 mA cm⁻²). In such demanding conditions, the battery lifespan is dramatically curtailed (20–40 cycles). Conventional factors associated with battery degradation, such as cathode degradation, transition metal dissolution, and gas generation,^{44–47} are identified as minimal contributor in the limited time. Instead, the battery degradation is directly linked to the lithium plating and stripping behaviors on the Cu current collector. Two typical failure behaviors are revealed: the AFE battery exhibits a “sudden-death” failure, predominantly due to uncontrolled accumulation of dead Li, whereas the LHCE battery displays a “gradual-decay” failure, largely stemming from SEI thickening. Evidently, compared to the dead Li-dominated sudden-death failure, AFLMBs following SEI-dominated gradual decay with reduced dead lithium offer extended lifespans and enhanced safety properties, showcasing a promising high-energy-density battery that potentially breaks the trad-off limitation among energy density, durability and safety. In addition, although LiH is detected in both

batteries during the cycling, its content remains relatively low up to the point of failure, reflecting that the formation of LiH is related to the electrolyte used but not a decisive factor in battery degradation. It is worthy of noting that the battery degradation behaviors revealed in the practical high-energy pouch cells are actually different from those in low-energy conditions (see Supplementary Table 1) due to two aspects of reasons. Firstly, for a low-energy AFLMB, like coin cell, with surplus electrolyte and thin cathode, the battery could run many cycles even at accumulation of dead Li as the dominant inactive Li, thus exhibiting a gradual decay but rather than sudden death.^{27,28,30} Secondly, the lifespan criterion for low-energy cells in previous reports (100% capacity loss) is different from high-energy pouch cells in this work (20% capacity loss). When reconsidering the lifespan of 20% capacity loss, all the low-energy AFLMBs in previous reports follow the SEI-dominated degradation (see Supplementary Table 1), which is likely caused by severe side reactions between low-CE electrolytes and Li metal. However, under the condition of 450 Wh kg⁻¹, low CE electrolytes (e.g. commercial carbonate-based electrolytes) fail to support reversible charge/discharge due to the dendritic short-circuiting (**Fig 7a.** and Supplementary Fig. 1). Therefore, the correlation between the inactive Li component and battery degradation behavior becomes more straightforward under practical high-energy pouch cells using high-CE electrolytes.

Secondly, the role of SEI in the failure of lithium metal batteries needs reevaluation under practical high-energy conditions. Prevailing perspectives hold that SEI rich in LiF, with stable chemical properties, good electronic insulation, and a high Young's modulus, can effectively inhibit lithium dendrite growth, facilitating uniform and dense deposition of lithium metal.^{2,7} However, our quantitative study on the SEI (**Fig. 6b–e**) reveals that the AFE-derived SEI contains more than twice the LiF content of the LHCE-derived SEI, and its Young's modulus is significantly higher. Yet, under 450 Wh kg⁻¹ condition, the AFE battery exhibits a faster growth rate of dead Li during cycling and a reduced lifespan, deviating from observations in lower-energy-density batteries. This discrepancy underscores the distinct SEI requirements for high-energy-density batteries. Notably, the SEI formed in AFE battery exhibits numerous microcracks even at the first complete discharge, worsening with each cycle, indicating that this LiF-rich SEI, despite its high Young's modulus, is not deformation-resistant.⁴⁸ In contrast, the LHCE battery presents a three-dimensional porous SEI structure without significant cracking over cycles, indicating a degree of flexibility afforded by the presence of highly

plastic N- and S-species.^{49,50} The brittle SEI in AFE battery is susceptible to cracking during lithium expansion/contraction cycles, causing extensive electrolyte contact with the lithium metal or Cu substrate. This leads to rapid electrolyte consumption and severe corrosion at the lithium deposit base, incrementally increasing contact impedance with the Cu substrate and fostering the formation of buried “truffle-shaped” dead Li, culminating in “sudden-death” degradation (**Fig. 7b**). On the other hand, the more flexible SEI in LHCE battery better accommodates volume change associated with lithium plating/stripping, which maintains structural integrity and consistent contact between the plated lithium and Cu during the cycling, thus, effectively suppressing the formation of dead Li. Accordingly, the capacity loss of battery predominantly depends on the rate of SEI thickening that is caused by the interface reaction between freshly plated lithium and the electrolyte, manifesting as a “gradual decay” failure (**Fig. 7c**). Furthermore, SEI thickening gradually consumes the initial lithium reservoir, reducing nucleation sites on Cu substrate and leading to the formation of “mushroom-shaped” lithium deposition morphology (**Fig. 7c**). Therefore, for high-energy-density batteries over 450 Wh kg⁻¹, where the thickness (or its volumetric changes) of the plated lithium layer is large, the flexibility of SEI becomes more critical than Young’s modulus for cycling stability.

Thirdly, the impact of the Cu substrate on battery failure demands more attention. Although both AFE and LHCE electrolytes achieve a CE exceeding 99% and a smooth lithium deposition in Li||Cu coin cells, the first deposition thickness under ultrahigh-capacity conditions (5.6 mAh cm⁻²) for the AFE and LHCE pouch cells reach 35.9 and 37.4 μm, respectively. These measurements significantly exceed the theoretical thickness of 29 μm, indicating the presence of significantly non-dense lithium deposition even in the first charging (**Fig. 7b,c**). Moreover, a distinctive “two-side” morphology characterizes the plated lithium metal layer in both batteries: the top surface displays dense and large-sized lithium grains, unlikely contributors to the non-dense deposition, whereas the bottom surface exhibits extensive porous lithium dendrites irrespective of the electrolyte used. This stark morphological contrast should be resulted from the intrinsic lithiophobic nature of the Cu substrate,^{16,23,51} hindering uniform lithium nucleation and growth, thereby causing non-dense lithium deposition in the first charge. Furthermore, this uneven lithium deposition at the bottom surface reduces the contact area between Cu and the plated lithium, inducing uneven current distribution, and deteriorating the quality of lithium deposition in subsequent cycles. Under the extreme conditions of

ultrahigh capacity deposition and minimal electrolyte dose, this adverse substrate effect, combined with the buildup of dead Li and SEI thickening, would further accelerate the degradation rate of 450 Wh kg⁻¹ AFLMBs. Therefore, the lithiophobic property of the Cu substrate also significantly impacts the lifespan of AFLMBs, highlighting the need for strategies to mitigate this adverse effect and enhance battery longevity.

Conclusions

In this work, we have performed a comprehensive study of the capacity degradation in >99% CE and Ah-level 450 Wh kg⁻¹ NCM811||Cu punch cells for the first time. Through the comprehensive analysis across cell, electrode, and atomic dimensions, the battery degradation is identified to be dominated by the anode side, and the correlation among the battery degradation behavior, lithium metal morphology evolution, dominant inactive component, and interphase properties is fully elucidated. In such high-energy-density batteries, where the volumetric change of the plated/stripped lithium is large, the flexibility of SEI emerges as a critical factor for cycling stability, overshadowing the traditionally emphasized parameters, like LiF/LiH content and Young's modulus. Two typical degradation modes are revealed: the brittle SEI is susceptible to cracking during cycling, which causes the formation of abundant "truffle-shaped" dead Li, and thus, resulting in "sudden-death" degradation; the flexible SEI better accommodates volume change, which effectively suppresses the dead Li formation and fosters a unique "mushroom-shaped" lithium deposition interwoven with thickened SEI, following a "gradual decay". Compared to the dead Li-dominated sudden-death failure, the SEI-dominated gradual decay, characterized by slower degradation and reduced dead lithium, demonstrates enhanced lifespan and safety. Consequently, to improve the lifespan of high-energy-density batteries, adoption of advanced electrolytes that can render flexible SEI becomes vital when the CE has been improved over 99%. Additionally, strategies for mitigating the adverse effect of lithiophobic Cu substrate are needed to improve the quality of initial lithium deposition. These findings illuminate the primary factors behind the performance degradation in high-energy-density scenarios (Ah-level 450 Wh kg⁻¹), distinguishing from the previous studies under lower-energy-density conditions and/or using lower CE electrolytes, thus providing essential guidance for developing cost-effective, durable, safe, and high-energy-density AFLMBs.

Acknowledgements

This work was supported by Research Center for Industries of the Future (RCIF) and Key Laboratory of 3D Micro/nano Fabrication and Characterization of Zhejiang Province at Westlake university, Westlake Education Foundation, and National Natural Science Foundation of China (Grant No. 21975207). The authors thank Dr. Yangjian Lin from Instrumentation and Service Center for Physical Sciences at Westlake University for supporting in Cryo-FIB-SEM measurements and data interpretation. Besides, the authors thank Drs. Lin Liu, Xiaohe Miao and Huang Zhang (from Instrumentation and Service Center for Physical Sciences), and Drs. Danyu Gu and Linyu Xiao (from Instrumentation and Service Center for Molecular Science) for their assistance in measurements at Instrumentation and Service Centers of Westlake University.

Author contributions

J.W. and L.L. designed the experiments. Y.X. carried out NMR measurements and guided L.L. for the titration experiments. L.L. fabricated the pouch cells and carried out all the other experiments. All authors contributed to the discussion, drawing and writing. J.W. conceived and led the project.

Competing interests

The authors declare no competing financial interests.

Additional information

Supplementary information is available online.

References

- 1 Lin, D.C., Liu, Y.Y. & Cui, Y. Reviving the lithium metal anode for high-energy batteries. *Nat. Nanotechnol.* **12**, 194-206 (2017).
- 2 Cheng, X.B., Zhang, R., Zhao, C.Z. & Zhang, Q. Toward safe lithium metal anode in rechargeable batteries: A Review. *Chem. Rev.* **117**, 10403-10473 (2017).
- 3 Liu, J. et al. Pathways for practical high-energy long-cycling lithium metal batteries. *Nat. Energy* **4**, 180-186 (2019).
- 4 Yamada, Y., Wang, J., Ko, S., Watanabe, E. & Yamada, A. Advances and issues in developing salt-concentrated battery electrolytes. *Nat. Energy* **4**, 269-280 (2019).
- 5 Qiao, Y., Deng, H., He, P. & Zhou, H.S. A 500 Wh/kg lithium-metal cell based on anionic redox. *Joule* **4**, 1445-1458 (2020).
- 6 Hobold, G.M. et al. Moving beyond 99.9% Coulombic efficiency for lithium anodes in liquid electrolytes. *Nat. Energy* **6**, 951-960 (2021).
- 7 Wan, H., Xu, J. & Wang, C. Designing electrolytes and interphases for high-energy lithium batteries. *Nat. Rev. Chem.* **8**, 30-44 (2023).
- 8 Nanda, S., Gupta, A. & Manthiram, A. Anode-free full cells: a pathway to high-energy density lithium-metal batteries. *Adv. Energy Mater.* **11**, 2000804 (2020).
- 9 Dong, L. et al. Toward practical anode-free lithium pouch batteries. *Energy Environ. Sci.* **16**, 5605-5632 (2023).
- 10 Fan, X. et al. Non-flammable electrolyte enables Li-metal batteries with aggressive cathode chemistries. *Nature Nanotechnol.* **13**, 715-722 (2018).
- 11 Ren, X.D. et al. Enabling high-voltage lithium-metal batteries under practical conditions. *Joule* **3**, 1662-1676 (2019).
- 12 Yu, Z. et al. Molecular design for electrolyte solvents enabling energy-dense and long-cycling lithium metal batteries. *Nat. Energy* **5**, 526-533 (2020).
- 13 Xue, W.J. et al. Ultra-high-voltage Ni-rich layered cathodes in practical Li metal batteries enabled by a sulfonamide-based electrolyte. *Nat. Energy* **6**, 495-505 (2021).
- 14 Lin, Y.F., Chen, J., Zhang, H. & Wang, J.H. In-situ construction of high-mechanical-strength and fast-ion-conductivity interphase for anode-free Li battery. *J. Energy Chem.* **80**, 207-214 (2023).
- 15 Mao, M.L. et al. Anion-enrichment interface enables high-voltage anode-free lithium metal batteries. *Nat. Commun.* **14**, 1082 (2023).
- 16 Lin, L.D. et al. Epitaxial induced plating current-collector lasting lifespan of anode-free lithium metal battery. *Adv. Energy Mater.* **11**, 2003709 (2021).
- 17 Oyakhire, S.T. et al. Electrical resistance of the current collector controls lithium morphology. *Nat. Commun.* **13**, 3986 (2022).
- 18 Wang, Y. et al. Anode-free lithium metal batteries based on an ultrathin and respirable interphase layer. *Angew. Chem.* **62**, e202304978 (2023).
- 19 Zhang, X.-L., Ma, L., Cai, Y.-P., Fransaer, J. & Zheng, Q. A low-Fermi-level current collector enables

- anode-free lithium metal batteries with long cycle life. *Matter* **7**, 583-602 (2024).
- 20 Louli, A.J. et al. Diagnosing and correcting anode-free cell failure via electrolyte and morphological analysis. *Nat. Energy* **5**, 693-702 (2020)..
- 21 Qiao, Y. et al. A high-energy-density and long-life initial-anode-free lithium battery enabled by a Li₂O sacrificial agent. *Nat. Energy* **6**, 653-662 (2021).
- 22 Lin, L. et al. Li-rich Li₂[Ni_{0.8}Co_{0.1}Mn_{0.1}]O₂ for anode-free lithium metal batteries. *Ange. Chem.* **60**, 8289-8296 (2021).
- 23 Liu, L. & Wang, J.H. Overcoming copper substrate thermodynamic limitations in anode-free lithium pouch cells via in situ seed implantation. *Nano Lett.* **23**, 10251-10258 (2023).
- 24 Gunnarsdóttir, A.B., Amanchukwu, C.V., Menkin, S. & Grey, C.P. Noninvasive NMR study of “dead lithium” formation and lithium corrosion in full-cell lithium metal batteries. *J. Am. Chem. Soc.* **142**, 20814-20827 (2020).
- 25 Niu, C. J. et al. Balancing interfacial reactions to achieve long cycle life in high-energy lithium metal batteries. *Nat. Energy* **6**, 723-732 (2021).
- 26 Zhou, M. Y. et al. Quantifying the apparent electron transfer number of electrolyte decomposition reactions in anode-free batteries. *Joule* **6**, 2122-2137 (2022).
- 27 Su, L., Charalambous, H., Cui, Z. & Manthiram, A. High-efficiency, anode-free lithium–metal batteries with a close-packed homogeneous lithium morphology. *Energy Environ. Sci.* **15**, 843-854 (2022).
- 28 Tao, M. M. et al. Quantifying the evolution of inactive Li/lithium hydride and their correlations in rechargeable anode-free Li batteries. *Nano Lett.* **22**, 6775-6781 (2022).
- 29 Tan, S. et al. Unravelling the convoluted and dynamic interphasial mechanisms on Li metal anodes. *Nat. Nanotechnol.* **18**, 243-249 (2022).
- 30 Xiang, Y. X. et al. Gas induced formation of inactive Li in rechargeable lithium metal batteries. *Nat. Commun.* **14**, 177 (2023).
- 31 Adhitama, E. et al. Assessing key issues contributing to the degradation of NCM-622||Cu cells: competition between transition metal dissolution and “dead Li” formation. *Adv. Energy Mater.* **14**, 2303468. (2024).
- 32 Li, H. Practical evaluation of Li-ion batteries. *Joule* **3**, 911-914 (2019).
- 33 Fang, C. C. et al. Pressure-tailored lithium deposition and dissolution in lithium metal batteries. *Nat. Energy* **6**, 987-994 (2021).
- 34 Shadike, Z. et al. Identification of LiH and nanocrystalline LiF in the solid-electrolyte interphase of lithium metal anodes. *Nat. Nanotechnol.* **16**, 549-554 (2021).
- 35 Chen, L. et al. Achieving high energy density through increasing the output voltage: a highly reversible 5.3 V battery. *Chem* **5**, 896-912 (2019).
- 36 Wang, J. H. et al. Fire-extinguishing organic electrolytes for safe batteries. *Nat. Energy* **3**, 22-29, (2018).
- 37 Cao, X. et al. Monolithic solid–electrolyte interphases formed in fluorinated orthoformate-based electrolytes minimize Li depletion and pulverization. *Nat. Energy* **4**, 796-805 (2019).
- 38 Lu, Y. Y., Tu, Z. Y. & Archer, L. A. Stable lithium electrodeposition in liquid and nanoporous solid electrolytes. *Nat. Mater.* **13**, 961-969 (2014).

- 39 Liu, Y. J. *et al.* Self-assembled monolayers direct a LiF-rich interphase toward long-life lithium metal batteries. *Science* **375**, 739 (2022).
- 40 Zachman, M. J., Tu, Z. Y., Choudhury, S., Archer, L. A. & Kourkoutis, L. F. Cryo-STEM mapping of solid-liquid interfaces and dendrites in lithium-metal batteries. *Nature* **560**, 345 (2018).
- 41 Xu, G.J. *et al.* The formation/decomposition equilibrium of LiH and its contribution on anode failure in practical lithium metal batteries. *Angew. Chem.* **60**, 7770-7776 (2021).
- 42 Xiang, Y.X. *et al.* Quantitatively analyzing the failure processes of rechargeable Li metal batteries. *Science Adv.* **7**, eabj3423 (2021).
- 43 Vilá, R.A. *et al.* LiH formation and its impact on Li batteries revealed by cryogenic electron microscopy. *Science Adv.* **9**, eadf3609 (2023).
- 44 Zhan, C., Wu, T., Lu, J. & Amine, K. Dissolution, migration, and deposition of transition metal ions in Li-ion batteries exemplified by Mn-based cathodes – a critical review. *Energy Environ. Sci.* **11**, 243-257 (2018).
- 45 Wang, J.H. *et al.* Concentrated electrolytes widen the operating temperature range of lithium-ion batteries. *Adv. Sci.* **8**, e2101646 (2021).
- 46 Wang, J.H. *et al.* Superconcentrated electrolytes for a high-voltage lithium-ion battery. *Nat. Commun.* **7**, 12032 (2016).
- 47 Myung, S.-T. *et al.* Nickel-rich layered cathode materials for automotive lithium-ion batteries: achievements and perspectives. *ACS Energy Lett.* **2**, 196-223 (2016).
- 48 He, M., Guo, R., Hobold, G.M., Gao, H. & Gallant, B.M. The intrinsic behavior of lithium fluoride in solid electrolyte interphases on lithium. *Proc. Natl. Acad. Sci. USA* **117**, 73-79 (2020).
- 49 Sakuda, A., Hayashi, A., Takigawa, Y., Higashi, K. & Tatsumisago, M. Evaluation of elastic modulus of Li₂S–P₂S₅ glassy solid electrolyte by ultrasonic sound velocity measurement and compression test. *J. Ceram. Soc. Jpn.* **121**, 946-949 (2013).
- 50 Cheng, D.Y. *et al.* A free-standing lithium phosphorus oxynitride thin film electrolyte promotes uniformly dense lithium metal deposition with no external pressure. *Nat. Nanotechnol.* **18**, 1448-1455 (2023).
- 51 Yan, K. *et al.* Selective deposition and stable encapsulation of lithium through heterogeneous seeded growth. *Nat. Energy* **1**, 16010 (2016).

Supporting Information for

From cell to atomic level: Understanding the Degradation in 99% Coulombic Efficiency and 450 Wh kg⁻¹ Anode-Free Pouch Cells

Lei Liu^{2,4,5} Yuxuan Xiang^{1,4*} and Jianhui Wang^{1,2,3,4*}

¹Research Center for Industries of the Future (RCIF), Westlake University, Hangzhou 310030, China.

²Key Laboratory of 3D Micro/Nano Fabrication and Characterization of Zhejiang Province, School of Engineering, Westlake University, Hangzhou 310030, China.

³Division of Solar Energy Conversion and Catalysis at Westlake University, Zhejiang Baima Lake Laboratory Co. Ltd., Hangzhou 310000, China

⁴Institute of Advanced Technology, Westlake Institute for Advanced Study, Hangzhou 310024, China.

⁵School of Materials Science and Engineering, Zhejiang University, Hangzhou, 310027, China.

*Corresponding Author: Yuxuan Xiang, Jianhui Wang

xiangyuxuan@westlake.edu.cn; wangjianhui@westlake.edu.cn

Experimental

Electrolyte preparation. Lithium bis(fluorosulfonyl)imide (LiFSI), lithium hexafluorophosphate (LiPF₆), fluoroethylene carbonate (FEC), 3,3,3-fluoroethylmethyl carbonate (FEMC), and 1,2-Dimethoxyethane (DME) and commercial electrolyte (CME, 1.0 M LiPF₆ in EC/DMC) were purchased from Duoduo Chem. 1,1,2,2-tetrafluoroethyl-2,2,2-trifluoroethyl ether (HFE) and 1,1,2,2-tetrafluoroethyl-2,2,3,3-tetrafluoropropyl ether (TTE) was purchased from Tokyo Chemical Industry Co.. The LHCE electrolyte was prepared by dissolving 1.5 M LiFSI in DME/TTE (molar ratio = 1.2 : 3). The AFE electrolyte was prepared by dissolving 1.0 M LiPF₆ in FEC/FEMC/HFE (weight ratio = 2 : 6 : 2). Electrolytes were prepared and stored in an argon-filled glovebox (Mikrouna, oxygen <0.1 ppm, water <0.1 ppm) at room temperature.

Anode-free lithium metal pouch cells construction. Cu||NCM811 anode-free lithium pouch cell was assembled using double coated single crystal Li[Ni_{0.8}Mn_{0.1}Co_{0.1}]O₂ (NCM811, 5.6 mAh cm⁻²) as the cathode, commercial polyethylene (PE) as the separator, and bare Cu foil without any surface coating as the anode. All pouch cells were filled with 2.0 g Ah⁻¹ electrolyte and vacuum sealing in an argon glovebox. Detailed cell parameters are provided in **Supplementary Table 1**.

Electrochemical measurements. The Coulombic efficiency (CE) tests were conducted on an NEWARE battery tester (NEWARE CT-4008-5V-10 mA) using Li||Cu coin cells. During cycling, 1.0 mAh cm⁻² Li was plated on Cu and was then stripped to 1.5 V at 0.2 mA cm⁻². All anode-free pouch cells were conducted within a voltage window of 2.8-4.4 V under galvanostatic charge–discharge cycling tests using NEWARE battery tester (NEWARE CT-4008-5V-6A) at 25 °C. The constant-voltage charge process was applied until the charge current decayed to C/20. After two formation cycles at C/10 rates, the cycle testing was performed at charge and discharge current densities of 1.12 mA cm⁻² and 2.8 mA cm⁻², respectively, corresponding to C/5 and C/2 current rates. Electrochemical impedance spectroscopy (EIS) tests were performed with a MPG-2 electrochemical workstation (Bio-Logic, France), amplitude for 10 mV in the frequency range from 100 mHz to 100 kHz.

Materials characterizations. All lithium plated/stripped samples for characterizations were rinsed using DME or DEC/DMC mixed solvent for three times to remove residual electrolytes. To avoid exposure to air and moisture, all samples were proceeded in a transfer device under argon atmosphere.

Field emission scanning electron microscope imaging (FE-SEM). The morphologies of top and bottom view of the plated Li were characterized using a field emission scanning electron microscope imaging (FE-SEM) on the SU8230, Hitachi, Ltd. The operating voltage and emission current of the electron beam were 5 kV and 10 μA, respectively.

Cryogenic focused ion beam scanning electron microscope (Cryo-FIB-SEM). The cross-sectional morphology of the plated Li layer were characterized using an Cryo-FIB-SEM on the Helios 5 UX, Thermo Fisher. The operating voltage and emission current of the electron beam were 5 kV and 0.2 nA, respectively. A gallium-ion beam source was used to mill the sample. The operating voltage of the ion-beam source was 30 kV. Different emission currents of the ion beam were chosen for different purposes, that is, 2 nA for pattern milling, 26 pA for imaging by the ion beam and 0.2 nA for cross-section cleaning. During ion-beam milling, the stage temperature was maintained at -195 °C to prevent beam damage on the plated Li sample.

Powder X-ray diffractometer (XRD). The structural information of SEI samples was conducted using XRD with Cu K α radiation ($\lambda=1.54178\text{ \AA}$) over a 2θ range of 10-80° with a step size of 0.02° (D8 Advance, Bruker). All samples for XRD characterization were placed in a BTUKER airtight specimen holder filled with pure argon.

X-ray photoelectron spectrometer (XPS). The surface elemental analysis was performed on the XPS with Al-K α radiation (Escalab 250Xi, Thermo Fisher). A charge neutralizer was applied to compensate for the sample surface charge. The binding energy was calibrated using F 1s peaks (684.9 eV) of LiF.

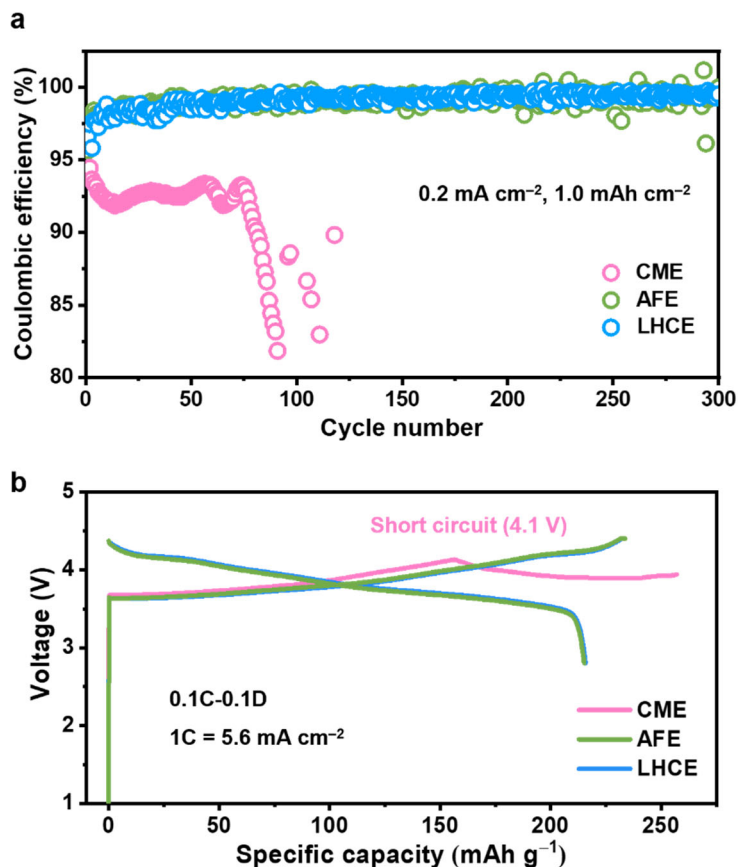
Solid state nuclear magnetic resonance (ssNMR). ^7Li and ^{19}F Magic Angle Spinning (MAS) NMR experiments were performed on a Bruker-AVANCE-500M NMR spectrometer (11.74 T) with the ^7Li Larmor frequency of 194.3 MHz and ^{19}F Larmor frequency of 470.4 MHz using a 1.3 mm double-resonance MAS probe. The samples were packed into 1.3 mm MAS rotors in argon-filled glove box and the sample spinning rate of 60 kHz was used during the measurements.

Atomic force microscope (AFM). AFM experiments were conducted on a Cypher ES, OXFORD Instruments under a protective gas atmosphere of pure argon. AM-FM module was chosen to measure the force mapping of SEI. Before the test, a standard sample of PVDF membrane with Young's modulus of 2.45 GPa was used to calibrate the probe.

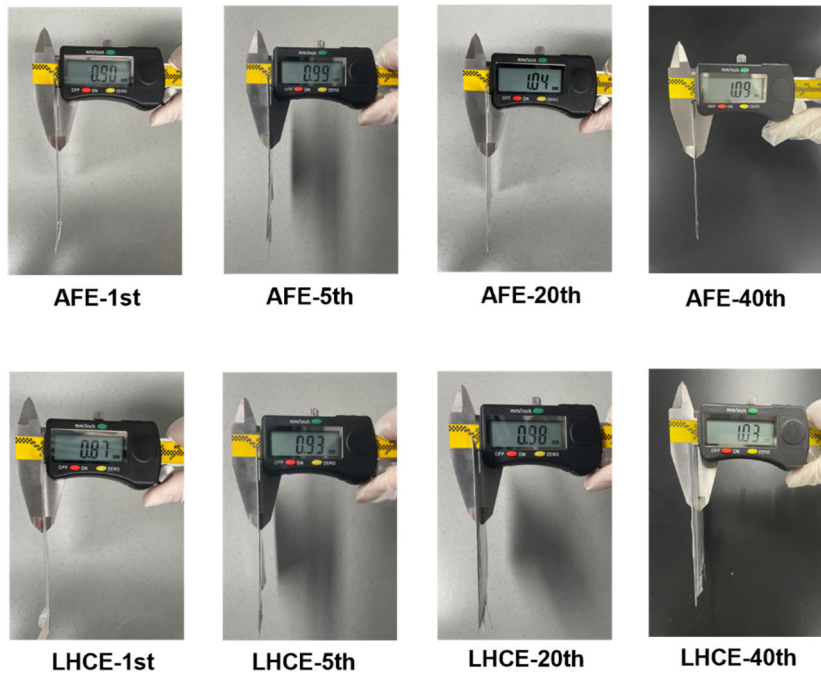
Inductively coupled plasma mass spectrometer (ICP-MS). Concentrations of transition metals in SEI samples were performed by ICP-MS (iCAP RQ, Thermo Fisher).

Mass spectrometry titration (MST). MST experiments were performed on a mass spectrometer (QAS 100, Shanghai Linglu) to quantify the amount of inactive metallic Li and LiH formed during cycling. The cycled Cu foils in a diameter of 16 mm were retrieved from anode-free pouch cells after full discharge to 1.0 V at 0.1C. These cycled Cu samples were put into a 5 ml bottle and sealed in the glove box. Upon MS detection, an excessive amount (0.5 ml) of D₂O (99.9%) was injected into the bottle and the residual inactive metallic Li and LiH reacted with the D₂O (99.9%) to form D₂ and HD

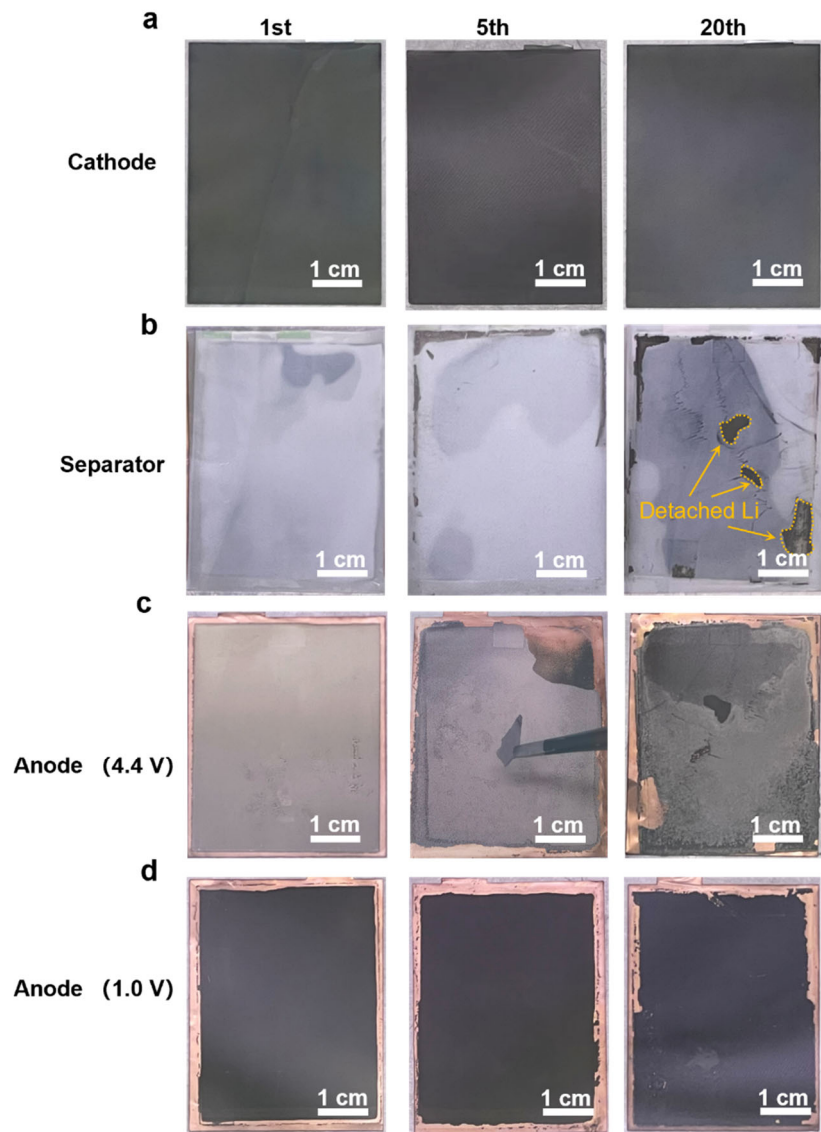
gas. Multiple-ion mode was used to record the ion current of mass/charge ratio (m/z) = 3 (for HD) and m/z = 4 (for D₂). After these signals fully attenuated, we integrated the signals of HD and D₂ and converted it into the mass of dead Li metal and LiH through the pre-established calibration curves shown in **Supplementary Fig. 12**. The establishment of calibration curves of dead Li and LiH was based on the MST tests of pure lithium metal and LiH with different mass (reference samples). An excellent linear relationship between the mass of Li or LiH with the corresponding gas signal was obtained, confirming the high precision of this MST method. As 1 mAh capacity loss corresponds to 0.25937 mg dead Li or 0.29674 mg LiH, the detected mass of dead Li and LiH can be further converted into the capacity loss, by which their contribution to the total capacity loss can be calculated.



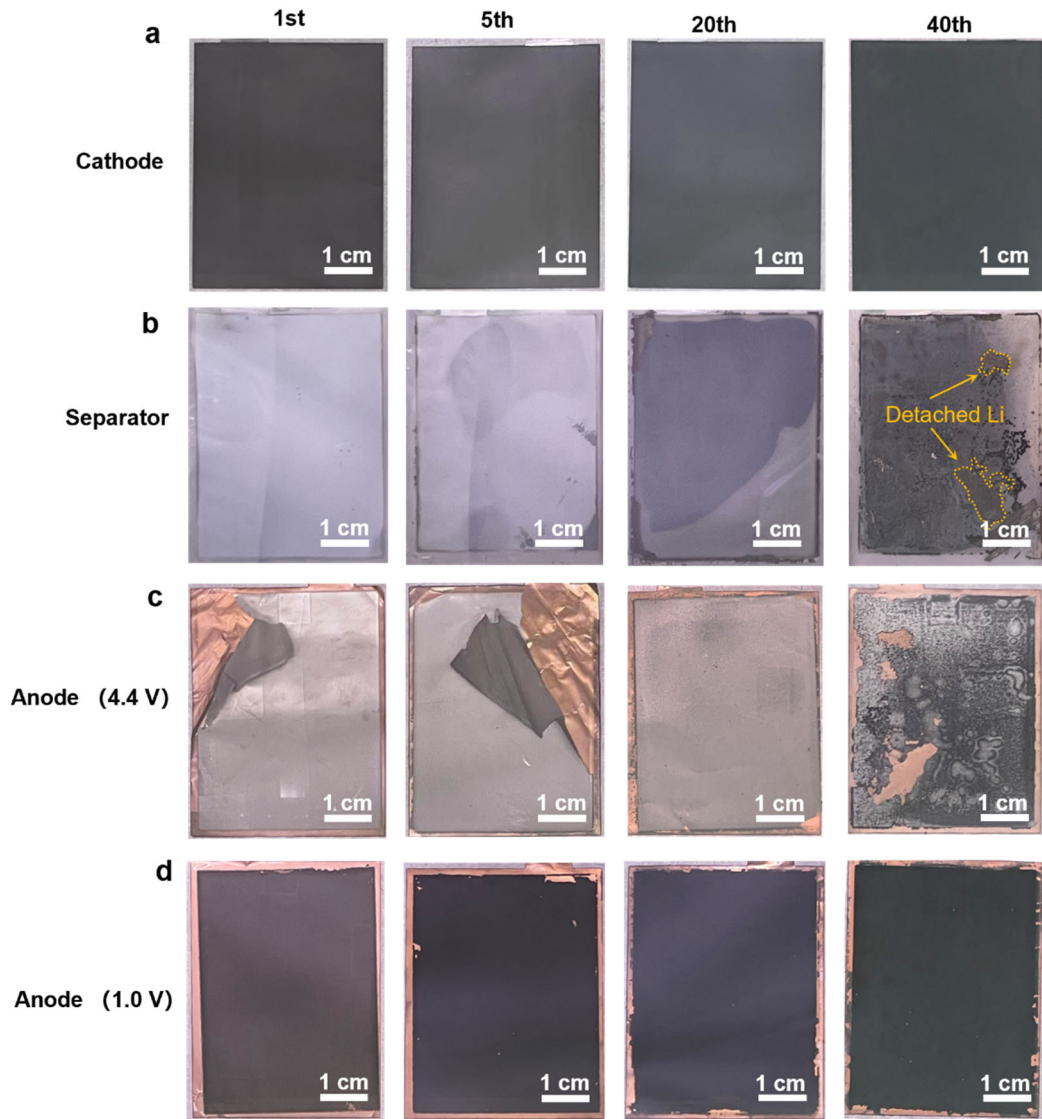
Supplementary Figure 1. Electrochemical performances in coin cells and pouch cells using electrolytes of AFE, LHCE and CME. (a) Coulombic efficiencies in Li||Cu coin cells using different electrolytes. (b) The first charge-discharge curves of 450 Wh kg⁻¹ anode-free lithium pouch cells using different electrolytes. Li||Cu coin cells consist of one Li chip (12.5 mm diameter), PE separator (19 mm diameter), and Cu foil (15 mm diameter). The amount of electrolyte was 60 µL per cell. The Coulombic efficiencies of Li||Cu coin cells were tested at 0.2 mA cm⁻² and 1.0 mAh cm⁻².



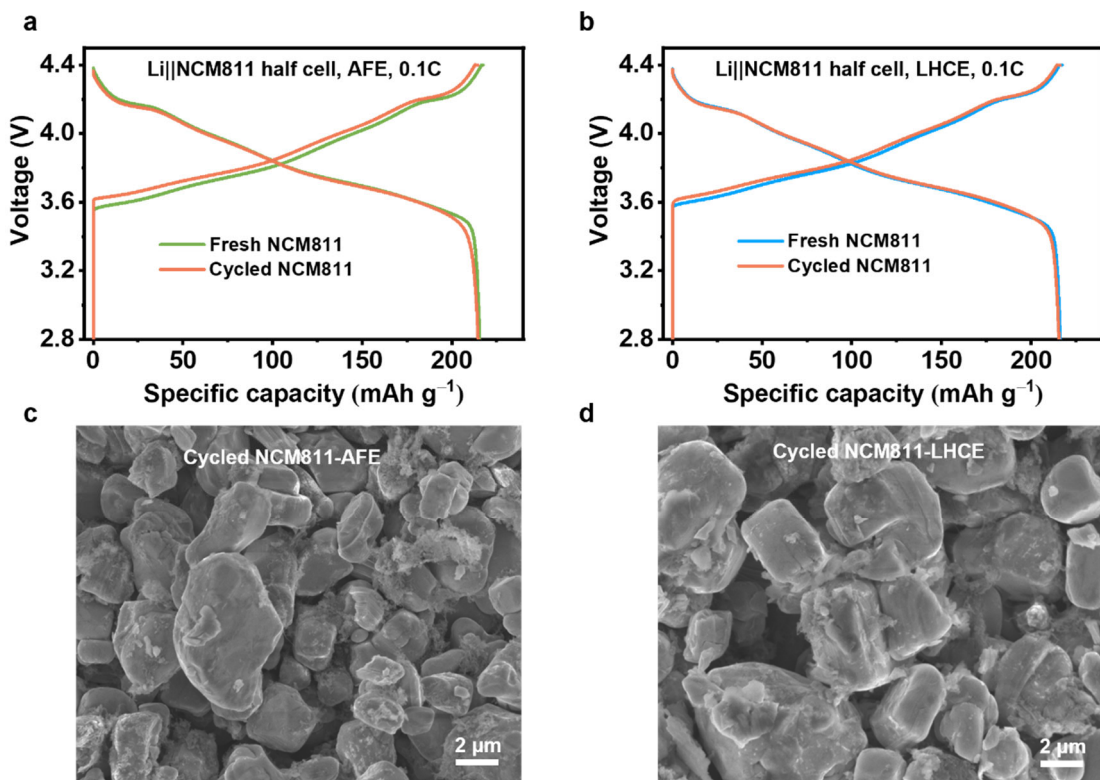
Supplementary Figure 2. Thickness variances of 450 Wh kg^{-1} AFLMBs at fully charged state (4.4 V) upon different cycles.



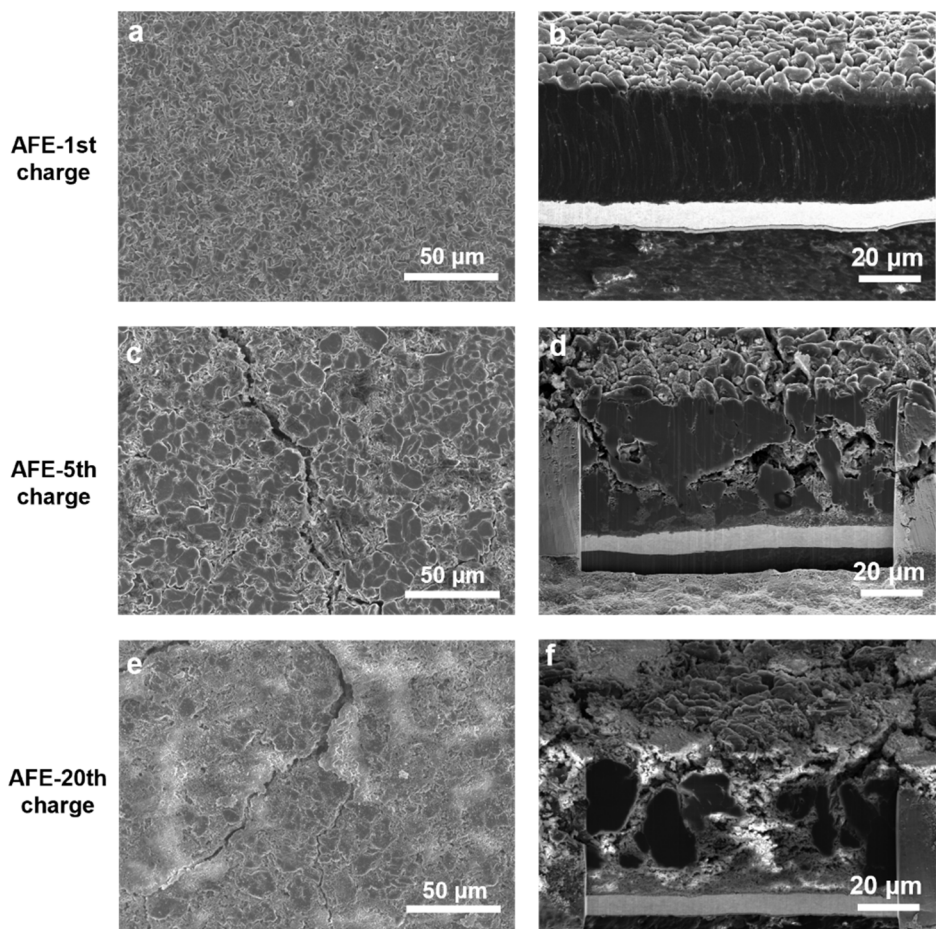
Supplementary Figure 3. Optical images of a disassembled AFLMB using AFE at different cycles. (a) Cathode, (b) Separator, (c) Anode at 4.4 V and (d) Anode at 1.0 V.



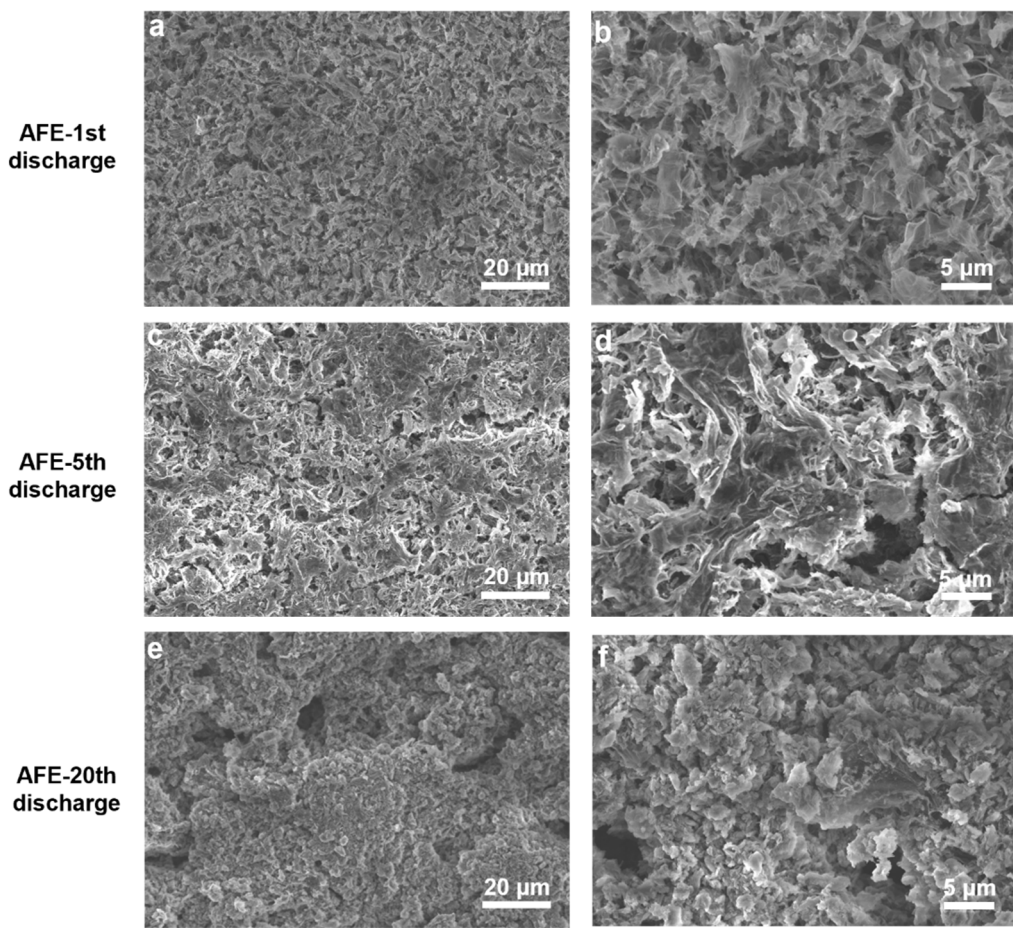
Supplementary Figure 4. Optical images of a disassembled AFLMB using LHCE at different cycles. (a) Cathode, (b) Separator, (c) Anode at 4.4 V and (d) Anode at 1.0 V.



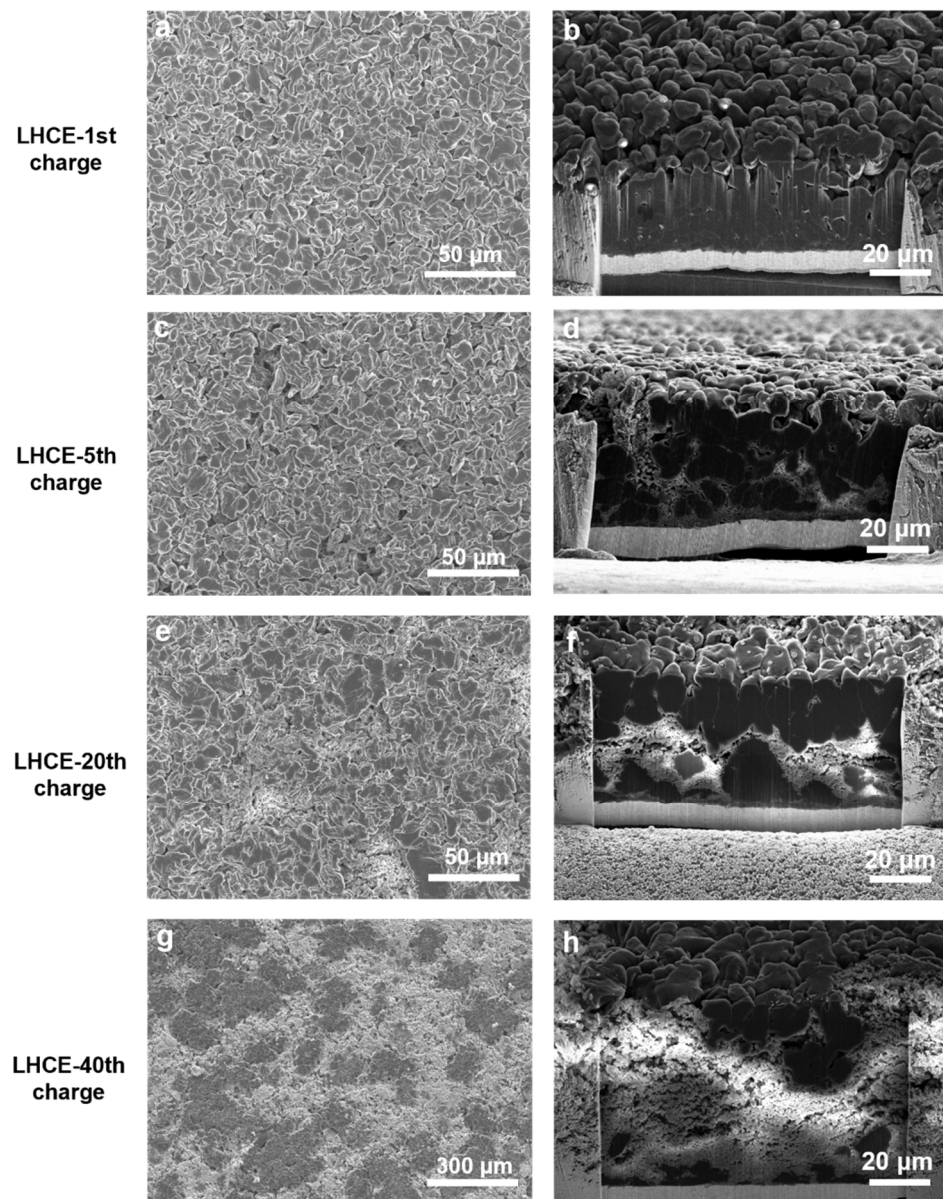
Supplementary Figure 5. Comparison between fresh NCM811 and cycled NCM811 retrieved from failed pouch cells with 20% capacity loss. (a, b) Charge-discharge curves of fresh NCM811 and cycled NCM811 in (a) AFE and (b) LHCE under the voltage window of 2.8~4.4 V. The cycled NCM811 cathode was retrieved from failed cells and re-assembled in a half-cell with fresh lithium anode and electrolyte. (c, d) SEM images of cycled NCM811 cathode retrieved from failed pouch cells using (c) AFE and (d) LHCE.



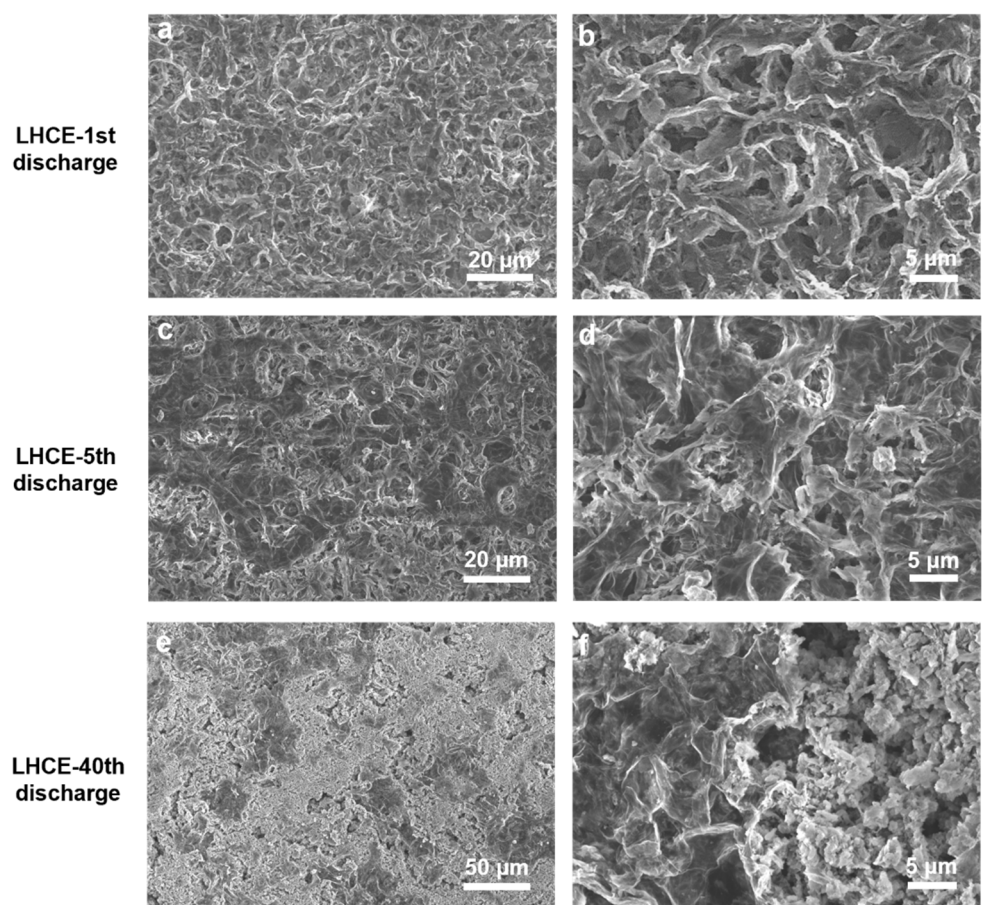
Supplementary Figure 6. Morphology evolution of deposited Li on the Cu current collector in the fully charged AFE-based AFLMB at different cycles. SEM images of top view: (a) 1st charge, (c) 5th charge, and (e) 20th charge. Cryo-FIB-SEM images of cross-section view: (b) 1st charge, (d) 5th charge, and (f) 20th charge.



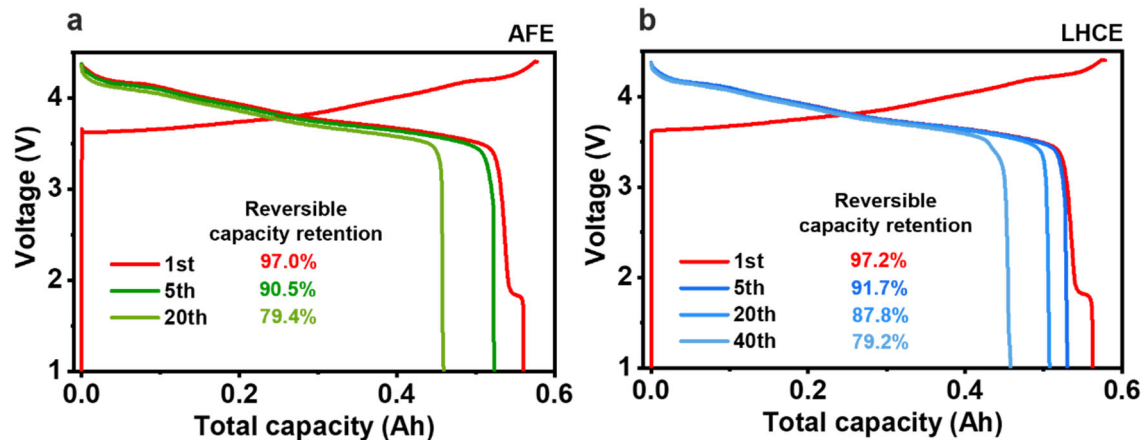
Supplementary Figure 7. Morphology evolution of stripped Li on the Cu current collector in the fully discharged AFE-based AFLMB at different cycles. (a, b) 1st discharge, (c, d) 5th discharge, and (e, f) 20th discharge.



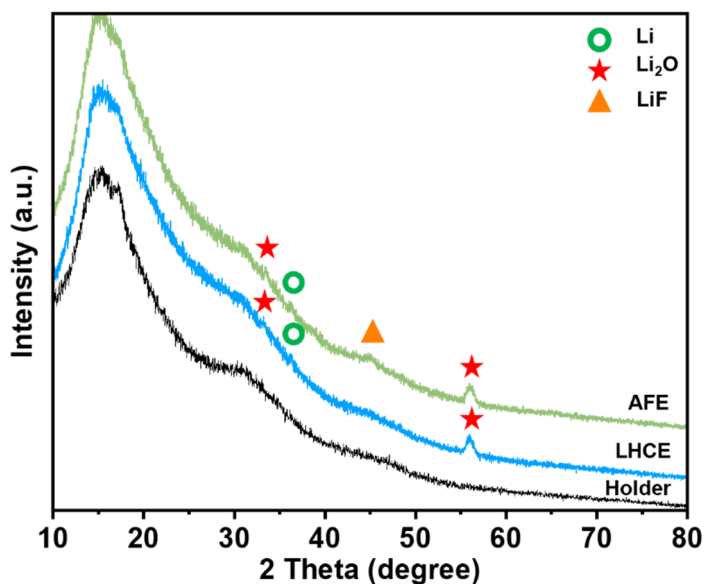
Supplementary Figure 8. Morphology evolution of deposited Li on the Cu current collector in the fully charged LHCE-based AFLMB at different cycles. SEM images of top view: (a) 1st charge, (c) 5th charge, (e) 20th charge, and (g) 40th charge. Cryo-FIB-SEM images of cross-section view: (b) 1st charge, (d) 5th charge, (f) 20th charge, and (h) 40th charge.



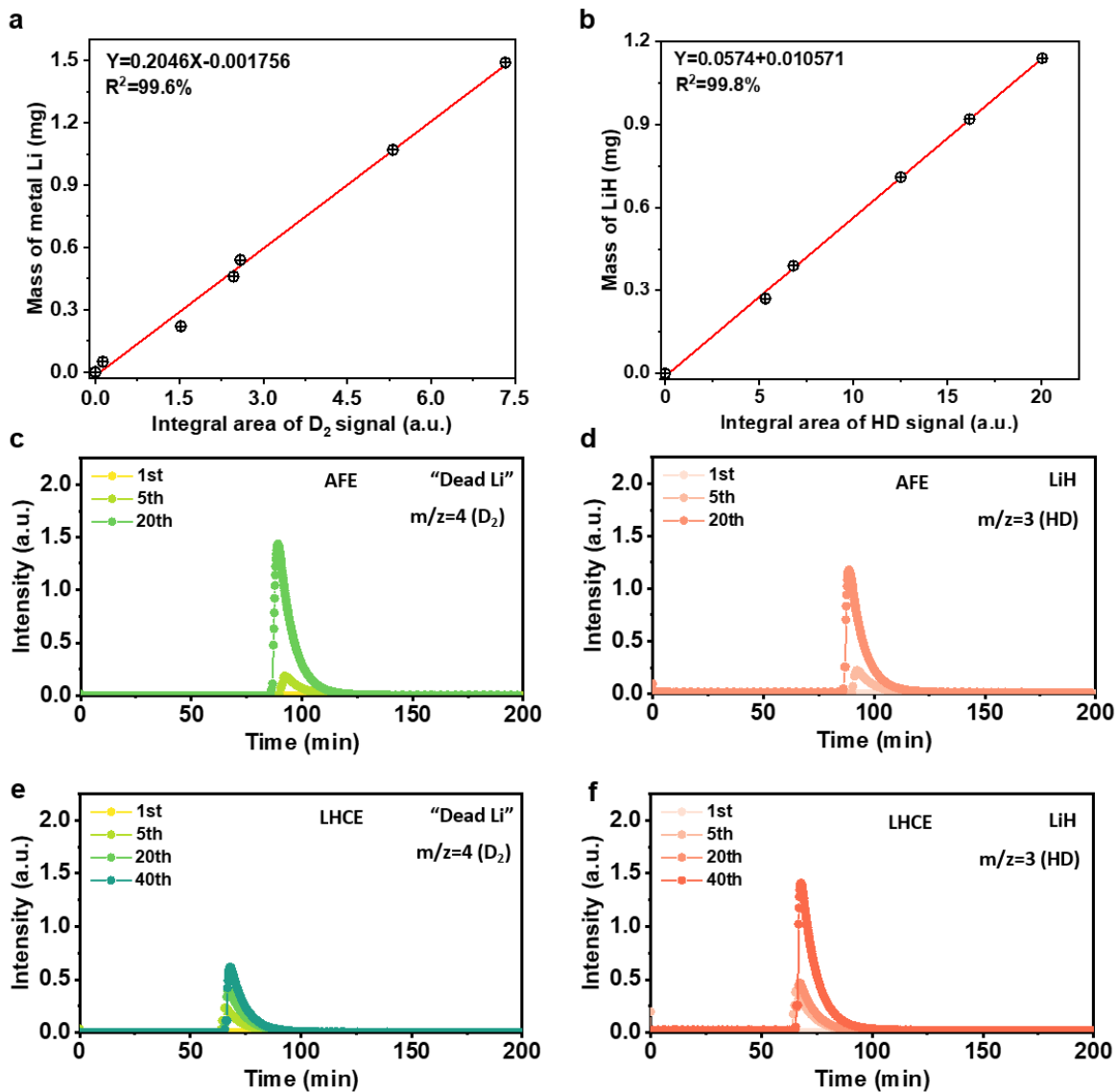
Supplementary Figure 9. Morphology evolution of stripped Li on the Cu current collector in the fully discharged LHCE-based AFLMB at different cycles. (a, b) 1st discharge, (c, d) 5th discharge, and (e, f) 40th discharge.



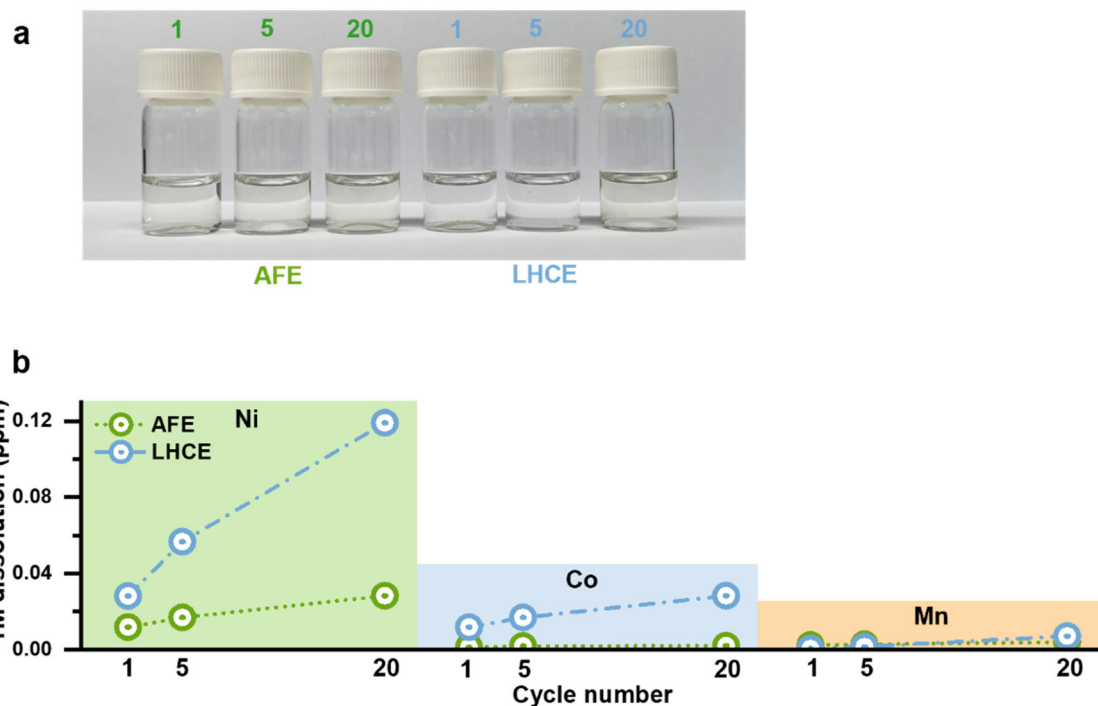
Supplementary Figure 10. Reversible capacity retention of 450 Wh kg⁻¹ AFLMBs at different cycles. (a) AFE and (b) LHCE. The reversible capacity retention is evaluated by the ratio of the discharged capacity at 1.0 V during the cycling to the 1st charged capacity at 4.4 V.



Supplementary Figure 11. XRD patterns of “ten milligram-level” SEI samples collected from 450 Wh kg⁻¹ AFLMBs after 5 cycles.



Supplementary Figure 12. Quantitative compositional analysis of inactive lithium by Mass spectrometry titration measurements. (a) Calibration curves of mass of Li metal in mg versus detected D_2 peak area. (b) Calibration curves of mass of LiH in mg versus detected HD peak area. (c, d) Evolution of D_2 (c) and HD (d) signals in the inactive Li analysis for the AFE-based AFLMB at different cycles. (e, f) Evolution of D_2 (e) and HD (f) signals in the inactive Li analysis for the LHCE-based AFLMB at different cycles.



Supplementary Figure 13. Transition metal contents in the SEI samples collected at different cycles. (a) Optical images of SEI dissolved in water. SEI was collected from 450 Wh kg⁻¹ AFLMBs after 1st, 5th, and 20th cycles. (b) ICP-MS results of Ni, Co, and Mn contents in the SEI samples.

Supplementary Table 1 Summary of representative failure studies of anode-free lithium coin cells and pouch cells.

References	Energy density (Battery type)	Cell parameter	CE	Electrolytes	Research scope	Characterization techniques	Failure mechanisms				
1. Nat. Energy 2020	<300 Wh kg ⁻¹ (Cu NCM523 Pouch cell)	2.8 mAh cm ⁻² 2.6 g Ah ⁻¹	98.3%	2.0 M LiDFOB+1.4 M LiBF ₄ in FEC/DEC	Cell, anode	NMR, X-ray CT, Ultrasonic mapping	Electrolyte depletion→degradation				
2. J. Am. Chem. Soc. 2020	<50 Wh kg ⁻¹ (Cu LFP Coin cell)	1.0 mAh cm ⁻²	92.0%	1.0 M LiPF ₆ in EC/DMC	Anode, interphase	In-situ NMR	Li metal corrosion→SEI→degradation (in 5 cycles)				
		>50 g Ah ⁻¹	98.0%	1.0 M LiPF ₆ in EC/DMC/FEC							
3. Nat. Energy 2021	350 Wh kg ⁻¹ (Cu NCM622 Pouch cell)	4.0 mAh cm ⁻² 2.6 g Ah ⁻¹	99.3%	LiFSI-1.2DME-3TTE	Cell, cathode, anode	SEM, STEM	Continuous loss of active Li→gradual decay				
4. Joule 2022	<50 Wh kg ⁻¹ (Cu NCM523 Coin cell)	2.7 mAh cm ⁻² >8 g Ah ⁻¹	99.0%	LiFSI:1.5DMC:2.0HFE	Anode, interphase	NMR	Solvation change→destabilized interphase→degradation				
5. Energy Environ. Sci. 2022	<50 Wh kg ⁻¹ (Cu NMCAM Coin cell)	1.6 mAh cm ⁻² >50 g Ah ⁻¹	95.0%	1.0 M LiPF ₆ in EC/EMC+2% VC	Anode	Operando XRD	Dead crystalline Li buildup→degradation				
			98.0%	0.6 M LiDFOB+0.6 M LiBF ₄ in FEC/DEC							
			99.3%	LiFSI-1.2DME-3TTE							
6. Nat. Nanotechnol. 2023	<50 Wh kg ⁻¹ (Cu NCM811 Coin cell)	1.8 mAh cm ⁻² >50 g Ah ⁻¹	98.4%	1.0 M LiFSI in DME	Interphase, cross talk,	Synchrotron XRD and PDF	Large crystalline LiOH→active Li loss (LiOH+Li)→degradation				
7. Nat. Commun. 2023	<50 Wh kg ⁻¹ (Cu LFP Coin cell)	2.2 mAh cm ⁻² >50 g Ah ⁻¹	93.7%	1.0 M LiPF ₆ in EC/ EMC	Anode, interphase	NMR, MS-titration	C ₂ H ₄ gas→dendrite & dead Li→degradation				
			89.0%	1.0 M LiDFOB in EC/ EMC							
8. Adv. Energy Mater. 2024	<50 Wh kg ⁻¹ (Cu NCM622 Coin cell)	1.7 mAh cm ⁻² >50 g Ah ⁻¹	95.0%	1.0 M LiPF ₆ in EC/EMC+2% VC	Cross talk, anode	ICP, GC-BID	Transition metal dissolution→dead Li→degradation				
9. Sci. Adv. 2021	<50 Wh kg ⁻¹ (Cu LFP Coin cell)	1.3 mAh cm ⁻² >50 g Ah ⁻¹	92.0%	1.0 M LiPF ₆ in EC/EMC	Anode, interphase	NMR, MS-titration, TGC	~20% capacity loss	SEI→degradation	~100% capacity loss	Dead Li+SEI→degradation	
			98.0%	1.0 M LiPF ₆ in EC/EMC+10%FEC			SEI→degradation			SEI→degradation	
10. Nano Lett. 2022	<50 Wh kg ⁻¹ (Cu LFP Coin cell)	2.2 mAh cm ⁻² >50 g Ah ⁻¹	98.0%	1.0 M LiPF ₆ in EC/ EMC+10% FEC	Anode, interphase	NMR, MS-titration	~20% capacity loss	SEI→degradation	~100% capacity loss	LiH→SEI→degradation	
			89.0%	1.0 M LiDFOB in EC/ EMC			SEI→degradation			Dead Li→degradation	
			97.0%	1.0 M LiDFOB in FEC			SEI→degradation			SEI→degradation	
This work	450 Wh kg ⁻¹ (Cu NCM811 Pouch cell)	5.6 mAh cm ⁻² 2.0 g Ah ⁻¹	92.0%	1.0 M LiPF ₆ in EC/DMC	Cell, anode, cathode, cross talk, interphase	Cryo-FIB-SEM, MS-titration, NMR, AFM et. al.	~20% capacity loss	Establishing the “Interphase properties-Li deposition evolution-Degradation behavior” correlation under practical high-energy conditions for the first time			
			99.1%	1.0 M LiPF ₆ in FEC/FEMC/HFE				①: Low-CE electrolyte→dendritic Li→ short circuit			
			99.3%	LiFSI-1.2DME-3TTE				②: Brittle SEI→“truffle-shaped” dead Li→ dead Li dominated “sudden death”			
								③: Flexible SEI→“mushroom-shaped” active Li→ SEI dominated “gradual decay”			

Supplementary Table 2. Cell parameters of the anode-free lithium pouch cell.

Cell component	Parameter	value
NCM811 Cathode (including Al foil)	Reversible capacity	216 mAh g ⁻¹
	Active material loading	97.5%
	Area weight (each side)	25.84 mg cm ⁻²
	Area capacity (each side)	5.6 mAh cm ⁻²
	Electrode length (mm)	5.6 cm
	Electrode width (mm)	4.3 cm
	Thickness of Al foil	12 µm
	Weight	1359 mg
	Number of layers	2
Cu foil	Thickness	8 µm
	Weight	207.9 mg
	Number of layers	3
Separator	Thickness	12 µm
Electrolyte	E/C ratio	2.0 g Ah ⁻¹
Pouch cell	Average voltage	3.82 V
	Total capacity	0.54 Ah
	Stack energy	2.06 Wh
	Stack total weight	4.578 g
	Stack energy density	450 Wh kg ⁻¹

References

1. A. J. Louli, A. Eldesoky, R. Weber, M. Genovese, M. Coon, J. deGooyer, Z. Deng, R. T. White, J. Lee, T. Rodgers, R. Petibon, S. Hy, S. J. H. Cheng and J. R. Dahn, *Nat. Energy*, 2020, **5**, 693-702.
2. A. B. Gunnarsdóttir, C. V. Amanchukwu, S. Menkin and C. P. Grey, *J. A. Chem. Soc.*, 2020, **142**, 20814-20827.
3. C. J. Niu, D. Y. Liu, J. A. Lochala, C. S. Anderson, X. Cao, M. E. Gross, W. Xu, J. G. Zhang, M. S. Whittingham, J. Xiao and J. Liu, *Nat. Energy*, 2021, **6**, 723-732.
4. Zhou, M. Y.; Ding, X. Q.; Ding, J. F.; Hou, L. P.; Shi, P.; Xie, J.; Li, B. Q.; Huang, J. Q.; Zhang, X. Q.; Zhang, Q., *Joule* 2022, **6**, 2122-2137.
5. L. Su, H. Charalambous, Z. Cui and A. Manthiram, *Energy Environ. Sci.*, 2022, **15**, 843-854.
6. S. Tan, J.-M. Kim, A. Corrao, S. Ghose, H. Zhong, N. Rui, X. Wang, S. Senanayake, B. J. Polzin, P. Khalifah, J. Xiao, J. Liu, K. Xu, X.-Q. Yang, X. Cao and E. Hu, *Nat. Nanotechnol.*, 2022, **18**, 243-249.
7. Y. Xiang, M. Tao, X. Chen, P. Shan, D. Zhao, J. Wu, M. Lin, X. Liu, H. He, W. Zhao, Y. Hu, J. Chen, Y. Wang and Y. Yang, *Nat. Commun.*, 2023, **14**, 177.
8. E. Adhitama, F. Demelash, T. Brake, A. Arifiadi, M. Vahnstiege, A. Javed, M. Winter, S. Wiemers-Meyer and T. Placke, *Adv. Energy Mater.*, 2024, **14**, 2303468.
9. Y. X. Xiang, M. M. Tao, G. M. Zhong, Z. T. Liang, G. R. Zheng, X. Huang, X. S. Liu, Y. T. Jin, N. B. Xu, M. Armand, J. G. Zhang, K. Xu, R. Q. Fu and Y. Yang, *Sci. Adv.*, 2021, **7**, eabj3423.
10. M. M. Tao, Y. X. Xiang, D. H. Zhao, P. Z. Shan, Y. Sun and Y. Yang, *Nano Lett.*, 2022, **22**, 6775-6781.